RSC Advances

ROYAL SOCIETY OF CHEMISTRY

PAPER

View Article Online
View Journal | View Issue

Cite this: *RSC Adv.*, 2026, **16**, 30928

High-efficiency ultra-thin CIGSe solar cells: defect engineering and back-surface field design

Serap Yiğit Gezgin,[a] M. A. Basyooni-M. Kabatas *[bcd] and Hamdi Şükür Kiliç[e]

This study presents a comprehensive SCAPS-1D simulation of an ultra-thin CIGSe/CdS/i-ZnO/ITO solar cell with a 420 nm absorber layer, focusing on the influence of key physical parameters and back surface field engineering. The effects of acceptor doping density in CIGSe ($N_a = 10^{13}$ to 10^{18} cm^{-3}), interface defect density ($N_{i-t} = 10^{9}$ to 10^{18} cm^{-3}), bulk defect density ($N_t = 10^{12}$ to 10^{20} cm^{-3}), and electron affinity ($\chi = 4.35$–4.65 eV) were systematically investigated. Increasing N_a significantly enhanced device performance by strengthening the internal electric field and increasing the carrier concentration, thereby improving V_{oc}, fill factor, and efficiency. In contrast, elevated interface and bulk defect densities led to severe recombination losses and significant degradation of all photovoltaic parameters. Optimal band alignment was obtained at $\chi \approx 4.35$ eV, corresponding to a slight negative conduction-band offset that facilitates carrier transport and suppresses recombination. Recombination analysis showed stable performance of the radiative recombination coefficient over the range 10^{-16} to 10^{-8} cm^{3} s^{-1}, while Auger recombination became dominant at coefficients above 10^{-23} cm^{6} s^{-1}. Among the investigated back surface field layers, Cu_2O provided the best performance due to its wide band gap (2.2 eV) and strong back-surface electric field, yielding a maximum simulated efficiency of ~40.3% with $V_{oc} = 0.817$ V, $J_{sc} = 30.03$ mA cm^{-2}, and FF = 82.88%. Capacitance–voltage and Mott–Schottky analyses revealed that capacitance increases from 57.6 to 109.9 nF cm^{-2} with increasing N_a, and the built-in potential ranges from 0.80 to 1.32 V, confirming enhanced junction properties. These results provide practical guidelines for optimizing ultra-thin CIGSe solar cells through defect control, band alignment tuning, and back surface field design.

Received 5th April 2026
Accepted 26th May 2026

DOI: 10.1039/d6ra02870e

rsc.li/rsc-advances

1 Introduction

Semiconductors belonging to the I–III–VI$_2$ family, including $CuInSe_2$ (CIS) and the gallium-alloyed $CuIn_xGa_{1-x}Se_2$ (CIGS), play a crucial role as light-absorbing layers in thin-film solar cells. CIGS has emerged as the leading material in the thin-film solar cell industry, distinguished by its exceptional light-harvesting capability, with an absorption coefficient exceeding 10^5 cm^{-1}, and its outstanding structural and environmental stability.[1] The electronic band gap of CIGS can be tuned between 1.0 eV and 1.7 eV through variation of gallium content, "x", in $CuIn_{1-x}Ga_xSe_2$ composition, enabling precise control over its optoelectronic properties.[2] The naturally limited abundance of indium (In) in CIGS compounds imposes a significant economic constraint, thereby increasing the production costs of thin-film solar cells that use CIGS as the primary absorber layer. To overcome this problem, the thickness of the absorber layer can be reduced to below 500 nm, and semiconductor layers of this thickness are referred to as ultra-thin films.[3] Particularly in solar cell applications, ultra-thin films are favored to minimize material costs, facilitate the rapid transport of photogenerated electrons and holes to the electrodes, reduce the likelihood of carrier recombination, and ultimately improve device efficiency. In ultra-thin absorber layers, only a small fraction of photons is absorbed, limiting the generation of photoexcited charge carriers and reducing device performance. To address this issue, light-trapping techniques[2] or back-surface field (BSF) layers are used to improve efficiency.[4]

BSF layers are heavily p$^+$-doped and are placed between the back contact and p-type absorber layer, where they help support charge-carrier transport and improve device performance. By establishing a strong electric field at a p$^+$–p junction, these layers guide minority carriers (electrons) from the p-type absorber toward the depletion region, reducing their recombination at the back contact and enabling more efficient carrier collection.[4] Additionally, they enable the smooth transport of

---

[a] Department of Physics, Faculty of Science, University of Selcuk, 42031 Selcuklu, Konya, Turkey

[b] Department of Precision and Microsystems Engineering, Delft University of Technology, Mekelweg 2, 2628 CD, Delft, The Netherlands. E-mail: m.kabatas@tudelft.nl

[c] Institute of Nanotechnology (INT), Karlsruhe Institute of Technology (KIT), Kaiserstraße 12, 76131, Karlsruhe, Germany. E-mail: m.kabatas@kit.edu

[d] Department of Nanotechnology and Advanced Materials, Graduate School of Applied and Natural Science, Selçuk University, Konya, 42030, Turkey

[e] Department of Metallurgical and Materials Engineering, Faculty of Engineering, University of Dokuz Eylül, İzmir, Turkey

hole carriers from the absorber layer to the back contact, thereby improving overall charge collection. In solar cells, a variety of p^+ type BSF materials such as SnS, V_2O_5, PbS, Sb_2S_3, Cu_2O, CuO, and CuSCN, are widely utilized to assist carrier transport and contribute to improved device efficiency.[4–6] Kumar *et al.* modelled a CIGS solar cell with $CuAlO_2$, $CuSbS_2$, $FaSnI_3$, P_3HT BSF layers and calculated efficiencies of 24.61%, 23.39%, 23.34%, 24.28%, respectively.[7] In the different studies, Kumar *et al.* determined J_{sc} of 42.59 mA cm^{-2}, 40.40 mA cm^{-2} and 35.64 mA cm^{-2}, V_{oc} of 0.8 V, 0.92 V, and 0.99 V, FF of 80.38%, 83.34% and 87.91% and efficiency of 27.73%, 31.13%, and 31.08%, for a CIGS solar cell consisting of SCWT, Cu_2O and CBTS BSF layers, respectively.[8–10] Barman and Kalita achieved that efficiency of 24.22% with a 1.5 µm CIGS layer and a 0.15 µm PbS layer.[11] Rahma *et al.* reported an efficiency of 21.835 for a CIGS solar cell with a 50 nm-thick Sn_2S_3 BSF layer.[12] PV parameters of CIGS solar cell with CNGS BSF layer modeled by Oublal *et al.*, which are determined to be V_{oc} of 1.21 V, J_{sc} of 32.25 mA cm^{-2}, FF of 75.08%, and efficiency of 29.39%.[13]

In calculating solar cell efficiency, the crystal, defect, electrical, and optical characteristics of each layer play an important role. The SCAPS-1D (Solar Cell Capacitance Simulator-1D) program enables the estimation of solar cell efficiencies based on the physical properties of the layers.[13,14] Furthermore, the SCAPS-1D program is used to calculate the efficiencies of experimentally fabricated solar cells and to verify their performance. Photovoltaic (PV) parameters are determined by factors such as interface defects, band gap, film thickness, electron affinity, radiative recombination, and acceptor defect density, providing insight into how these variables influence solar cell performance.[15,16]

In this study, we modelled a solar cell using SCAPS-1D with a CIGSe absorber layer at 420 nm thickness that we previously produced using the PLD technique.[17] We have calculated the potential efficiency of a solar cell by considering factors such as electron affinity, interface defect density, acceptor defect density, recombination mechanisms, and capacitance. Furthermore, the performance of the CIGSe ultra-thin film solar cell was significantly improved by using heavily p^+-doped Sb_2S_3, CuO, and CuO_2 BSF layers. *C–V*, C^{-2}–*V*, and *C–f* characteristics were obtained as a function of the acceptor defect density. As a result, our findings provide insight into the expected performance of a CIGSe ultra-thin film solar cell with a thickness of 420 nm during experimental production.

2 The modeling of Au/BSF (Sb_2S_3, CuO, Cu_2O)/CIGSe/CdS/i-ZnO/ITO solar cell

Numerical simulations play a crucial role in elucidating the physical characteristics and optimizing the design of solar cells. The advancement of simulation techniques has enabled comprehensive pre-experimental analysis and optimization of solar cell efficiency and structural design. This work utilizes the SCAPS-1D simulation platform to investigate the performance of the CIGSe solar cell. The software, developed at ELIS, Ghent University, is a one-dimensional solar cell simulator available for researchers worldwide. SCAPS-1D enables the grading of a wide range of physical parameters, such as band gap energy, acceptor density, electron affinity, interface defect density, operating temperature, serial and shunt resistance, *etc.*[17–19]

A numerical model of Au/CIGSe/CdS/i-ZnO/ITO solar cell configuration was developed in SCAPS-1D (Fig. 1(b)), based on experimentally validated parameters obtained from our earlier investigation of a monocrystalline CIGSe absorber layer.[17] We predicted the PV response of the CIGSe solar cell model by analyzing the impact of varying defect-related, structural, and optical parameters, including N_{i-t}, N_a, χ_e, and B_r, *etc.* CIGSe semiconductor parameters derived from experimental measurements are given in Table 1, and the absorption coefficient spectrum of the ultra-thin film given in Fig. 1(c) was used as an input dataset in the simulation. The thin film thickness was measured at 420 nm, the band gap was determined from the Tauc plot in the small square shown in Fig. 1(c) as 1.37 eV, and carrier mobility was measured using the four-probe Hall effect. The physical parameters of all layers forming the solar cell were taken from the literature.[4,5,17,20,21] PV parameters were calculated under illumination conditions of 100 mW cm^{-2}. The *J–V* characteristic and band gap of the ideal solar cell modeled without BSF are given in Fig. 1(a). Sb_2S_3, CuO, and C_2O BSF layers were used to further increase the efficiency of a thin absorber solar cell.

In SCAPS, simulations can include as many as seven semiconductor layers, while the software solves the Poisson equation and carrier continuity equations

$$\frac{d^2}{dx^2}\Psi(x) = \frac{e}{\varepsilon_o \varepsilon_r} p(x) - n(x) + N_D - N_A + \rho_p - \rho_n \tag{1}$$

$$\begin{aligned} \frac{dJ_n}{dx} &= G - R \\ \frac{dJ_p}{dx} &= G - R \end{aligned} \tag{2}$$

for electrons and holes.[17,22] Where the parameters represented in these equations can be defined as below: $\Psi(x)$ defines the electrostatic potential, e is the elementary charge, ε_r and ε_0 denote relative and vacuum permittivity, p and n represent hole and electron concentrations, N_D and N_A indicate donor and acceptor impurity levels, and ρ_p and ρ_n describe hole and electron carrier distributions, R indicates the recombination rate, G represent generation rate.

The transport of electrons and holes in semiconductors is facilitated by drift and diffusion, which can be quantitatively described by eqn (3):

$$\begin{aligned} J_n &= D_n \frac{dn}{dx} + \mu_n n \frac{d\Phi}{dx} \\ J_p &= D_p \frac{dp}{dx} + \mu_p p \frac{d\Phi}{dx} \end{aligned} \tag{3}$$

2.1. The impact of the acceptor defect density (N_a) of the absorber layer

The acceptor carrier density (N_a) of the CIGSe absorber layer significantly affects the solar cell's efficiency. Optimization of

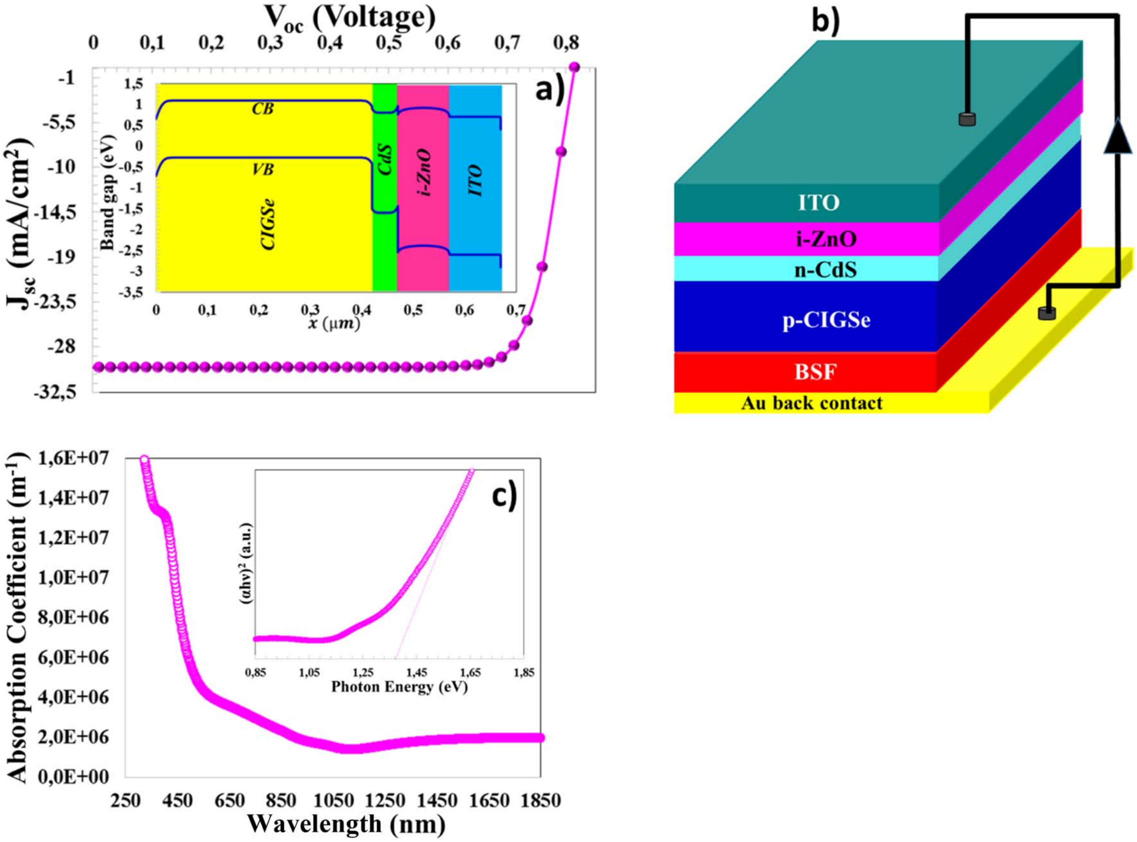

Fig. 1 (a) *J–V* characteristic (band diagram in insert square), and (b) the schematic view of CIGSe/CdS solar cell with Cu_2O BFS layer.

Table 1 Physical characteristics of the layers in the simulated $Cu_2ZnSnSe_4$ solar cell

Layers for solar cells	ITO[21]	i-ZnO[18]	CdS[20]	CIGSe[17]	$p^+Sb_2S_3$[5]	p^+ CuO[4]	p^+ Cu_2O[4]
Energy gap (eV)	3.3	3.3	2.4	1.37 (exp.)	1.62	1.51	2.2
Affinity of electron (eV)	4.6	4.6	4.2	Variable	3.7	4.07	3.2
The permittivity of dielectric	9	9	10	8.6	7.08	18.1	7.1
CB effective density (cm^{-3})	2.2×10^{18}	2.2×10^{18}	2.2×10^{18}	7.91×10^{17}	2.0×10^{19}	2.2×10^{19}	2.5×10^{18}
VB effective density (cm^{-3})	1.8×10^{19}	1.8×10^{19}	1.8×10^{19}	4.5×10^{18}	1×10^{19}	5.5×10^{20}	1.5×10^{19}
Thermal velocity of electron/hole (cm s^{-1})	1.0×10^7	1.0×10^7	1.0×10^7	1.0×10^7	1.0×10^7	1.0×10^7	1.0×10^7
Mobility of electron/hole (cm^2 V^{-1} s^{-1})	100/25	100/25	100/25	40/10 (exp.)	9.8/10	100/0.1	200/800
Density of shallow donor (cm^{-3})	1.0×10^{20}	1.0×10^5	1.0×10^{18}	0	0	0	0
Density of shallow acceptor (cm^{-3})	0	0	0	Variable	1.0×10^{15}	1.0×10^{18}	1.0×10^{18}
Thickness of film (nm)	100	100	50	420 (exp.)	Variable	Variable	Variable

the absorber doping level can be achieved through the strategic increase of acceptor defect density.[23,24] Enhanced doping levels increase the carrier density and the photogenerated carrier population, while defects introduce localized energy states that trap carriers; acceptor defects facilitate efficient carrier transfer. Introducing energy barriers for holes enhances carrier transport over long distances, while low-energy defect states act to form internal electric fields that guide carriers and reduce recombination losses,[25] A rise in acceptor defect density leads to higher saturation current levels and impacts V_{oc}, as illustrated in eqn (5), where the role of N_a reflects p-type doping influence:[26]

$$V_{oc} = \frac{k_B T}{q} \ln\left(\frac{np}{{n_i}^2}\right) \tag{5}$$

here, T indicates absolute temperature, q denotes the electron charge, and k_B represents the Boltzmann constant, while n and p correspond to the densities of photo-generated carriers and n_i defines the intrinsic carrier density. Higher N_a content in CIGSe thin film increases hole concentration, thereby enhancing carrier density and promoting charge accumulation in the depletion region. Increasing N_a concentration from 1×10^{13} cm^{-3} to 1×10^{18} cm^{-3}[27] resulted in considerable improvements in V_{oc}, FF, and efficiency, which rose from 0.298 V to 0.757 V,

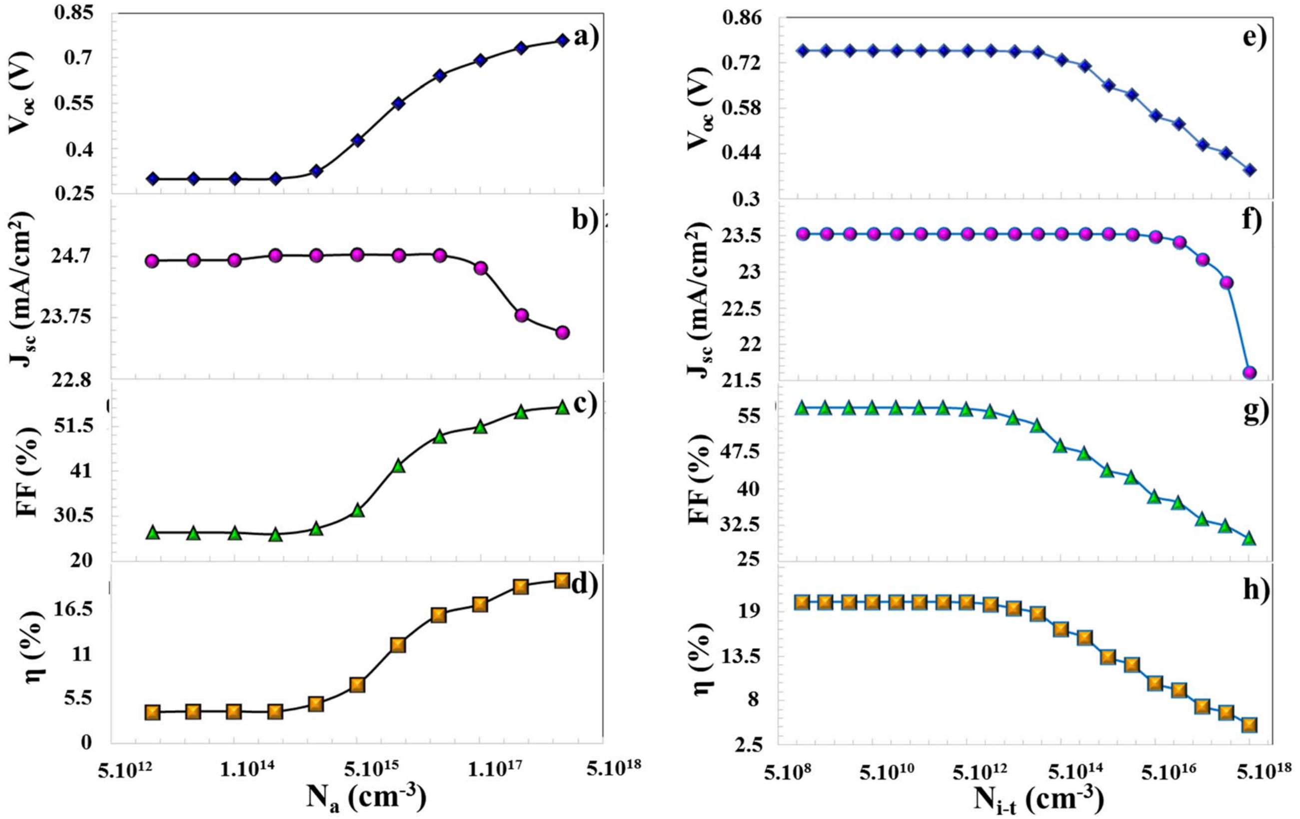

Fig. 2 Variation of PV parameters: V_{oc}, J_{sc}, FF, η as a function of (a–d) N_a (cm^{-3}) and (e–h) N_{i-t} (cm^{-3}).

26.78% to 55.97%, and 3.835% to 19.953%, respectively, as depicted in Fig. 2(a–d). This increase can be attributed to the higher hole density resulting from increased p-type doping levels, the strengthened internal electric field, and decreased carrier recombination. The increased acceptor density facilitated the collection of photo-generated carriers by enabling more efficient charge separation in the hole region. High N_a values increased band bending, reducing recombination losses in the back-contact direction for carriers and supporting charge transfer. However, the fact that the performance increase approached saturation at very high doping levels indicates that excessive defect density can limit carrier lifetime by forming recombination centers. In CIGSe thin films, acceptor-type defects are not expected to be distributed at a single energy level or in a homogeneous manner; instead, there is a spatially heterogeneous distribution of different energy levels (shallow and deep) in intragranular, grain boundary, and interface regions. The presence of deep-level traps can negatively impact carrier lifetime by creating additional Shockley–Read–Hall (SRH) recombination centers, partially offsetting the positive effect of increased doping.

2.2. The impact of the interface defect density (N_{i-t}) between CIGSe and CdS semiconductors

The formation of defect-induced energy levels at the interface affects how electrons and holes move across the absorber/buffer heterojunction.[28] At the interface, fundamental defects such as dangling bonds, vacancies, and interfacial states can form, leading to electron–hole recombination and perturbing the local electric field, while fabrication-related issues, such as thin-film deposition, epitaxial growth, and band mismatch, also contribute to defect formation. In thin-film solar cells, interface defects generally do not exhibit a single-level, homogeneous structure; instead, they display a spatially heterogeneous distribution of multi-level trap structures with shallow and deep energy levels. While low and medium-level interface defects can support charge transfer by regulating band alignment in certain situations, excessive defect density leads to the dominance of deep-level trap centers. These deep-level conditions strengthen the SRH recombination mechanism, thereby increasing the probability of interface electron–hole recombination. Furthermore, the non-homogeneous defect distribution creates local potential fluctuations at the absorber/buffer interface, limiting carrier transport and increasing the series resistance effect. The impact of interface defects is minimal within the N_{i-t} range of 1×10^9 to 1×10^{13} cm^{-3}, indicating that interface recombination is negligible and carrier transport occurs efficiently. In this region, the internal electric field generated along the heterojunction is conserved, and photo-generated carriers can be collected with minimal loss. However, increasing the defect density (from 5×10^{13} cm^{-3} to 5×10^{18} cm^{-3})[29] beyond this range significantly deteriorates PV parameters, the values of V_{oc}, J_{sc}, FF, and efficiency decreased significantly, dropping from 0.757 V to 0.389 V, 23.52 mA cm^{-2} to 21.60 mA cm^{-2}, 56.54% to

29.78%, and 20.16% to 5.00%, respectively, as shown in Fig. 2(e–h). Increased defect levels at the interface cause electrons and holes to recombine there, forming SRH recombination centers. The significant decrease in V_{oc}, in particular, is associated with a reduction in the carrier semi-Fermi level separation and an increase in the saturation current. The substantial decrease in FF can be attributed to increased charge-transfer resistance at the interface and decreased carrier-collection efficiency.

2.3. Impact of the conduction band offset (CBO)

The conduction band offset describes the energy difference between the conduction band minima of two semiconductors forming a heterojunction. Differences in electron affinity (χ) between semiconductor materials lead to conduction and valence band offsets, identified as CBO (ΔE_C) and VBO, which are described in eqn (6) and (7):[22]

$$\text{CBO} = \Delta E_C = \chi_{\text{absorber}} - \chi_{\text{buffer}} \tag{6}$$

$$\text{VBO} = (\chi_{\text{absorber}} + E_{\text{g absorber}}) - (\chi_{\text{buffer}} + E_{\text{g buffer}}) \tag{7}$$

The interfacial energy barrier between absorber and buffer layers significantly impacts carrier transport mechanisms. A positive conduction band offset ($\chi_{\text{abs}} > \chi_{\text{buff}}$) results in a spike-like barrier, which leads to recombination while restricting electron flow.[30] To cross the heterojunction interface, photogenerated electrons must use their kinetic energy to surmount the existing potential barrier. For $\chi_{\text{abs}} < \chi_{\text{buff}}$, the resulting negative CBO induces a cliff-type band configuration, associated with a reduced band discontinuity. As a result, photogenerated electrons can effectively surmount the interface barrier by utilizing their kinetic energy.

In the current study, device performance was analyzed as a function of the CIGSe electron affinity over the range $\chi = 4.35$–4.65 eV.[16,31] Elevating the electron affinity of CIGSe from $\chi = 4.35$ eV to 4.65 eV leads to the formation of a spike-like conduction band offset at the absorber–buffer interface[32] (Fig. 3(a)), impeding electron migration to CdS and promoting interfacial recombination losses. Spike-like (positive CBO) conduction band alignment creates an energy barrier for electrons at the absorber/buffer interface. In suitable (small and controlled) spike structures, this barrier can reduce interface recombination by restricting reverse carrier flow and can, in particular, increase V_{oc}. It also improves carrier selectivity and enhances diode quality by preventing uncontrolled electron passage across the interface. Furthermore, high spike values can slow down carrier extraction, increasing the series resistance effect. Conversion: the creation of an energy barrier that prevents electron transport at the interface. As the barrier height increases, it becomes more difficult for photogenerated electrons to pass into the buffer layer, leading to carrier accumulation at the interface and increased SRH recombination. A cliff-type band alignment corresponding to $\Delta E_c = -0.05$ eV is formed at $\chi = 4.35$ eV (Fig. 3(b)). The observed negative valence band offset ($\Delta E_v = -1.08$ eV) promotes a cliff-type band configuration that effectively suppresses the recombination of photo-excited carriers.[33] The cliff structure formed at slightly negative CBO values can reduce the band discontinuity between the absorber and buffer layers, providing a more favorable energy alignment at the interface. This can accelerate charge transfer by reducing carrier accumulation in some devices and by helping maintain the occupancy factor (FF). It has been reported that small negative or near-zero CBO values can create an optimal balance between electron transport and interface recombination. However, the cliff-type conduction-band alignment, while facilitating electron transport, leads to electron accumulation at the interface at excessively negative potentials (a deep cliff structure), increasing SRH recombination and causing V_{oc} losses. It can also weaken carrier selectivity, increasing reverse current and diode losses. The effect is more complex due to the non-homogeneity of interface defects in the device and the presence of multi-level energy states. Grain boundaries and chemical irregularities enhance carrier localization and recombination. Therefore, cliff-tip alignment can limit performance, especially at large negative CBO values. At an electron affinity of $\chi = 4.65$ eV, V_{oc}, J_{sc}, FF, and conversion efficiency drop to 0.458 V, 23.51 mA cm^{-2}, 40.03%, and 8.62%, respectively, highlighting the performance deterioration (Fig. 4(a–d)).

2.4. The generation and recombination mechanism

2.4.1. The impact of the defect density (N_t) in the absorber semiconductor. In CIGSe thin-film absorber layers, the defect

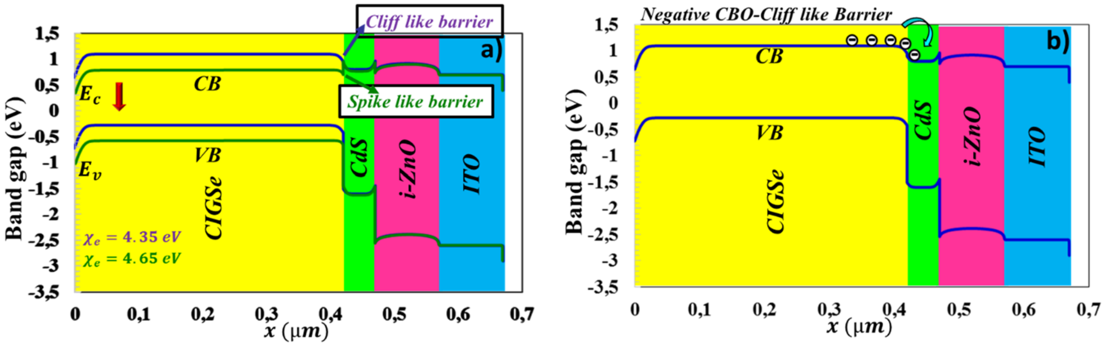

Fig. 3 (a) A comparative band alignment illustrating cliff-type and spike-type interfacial barriers, and (b) a negatively offset cliff-like barrier configuration.

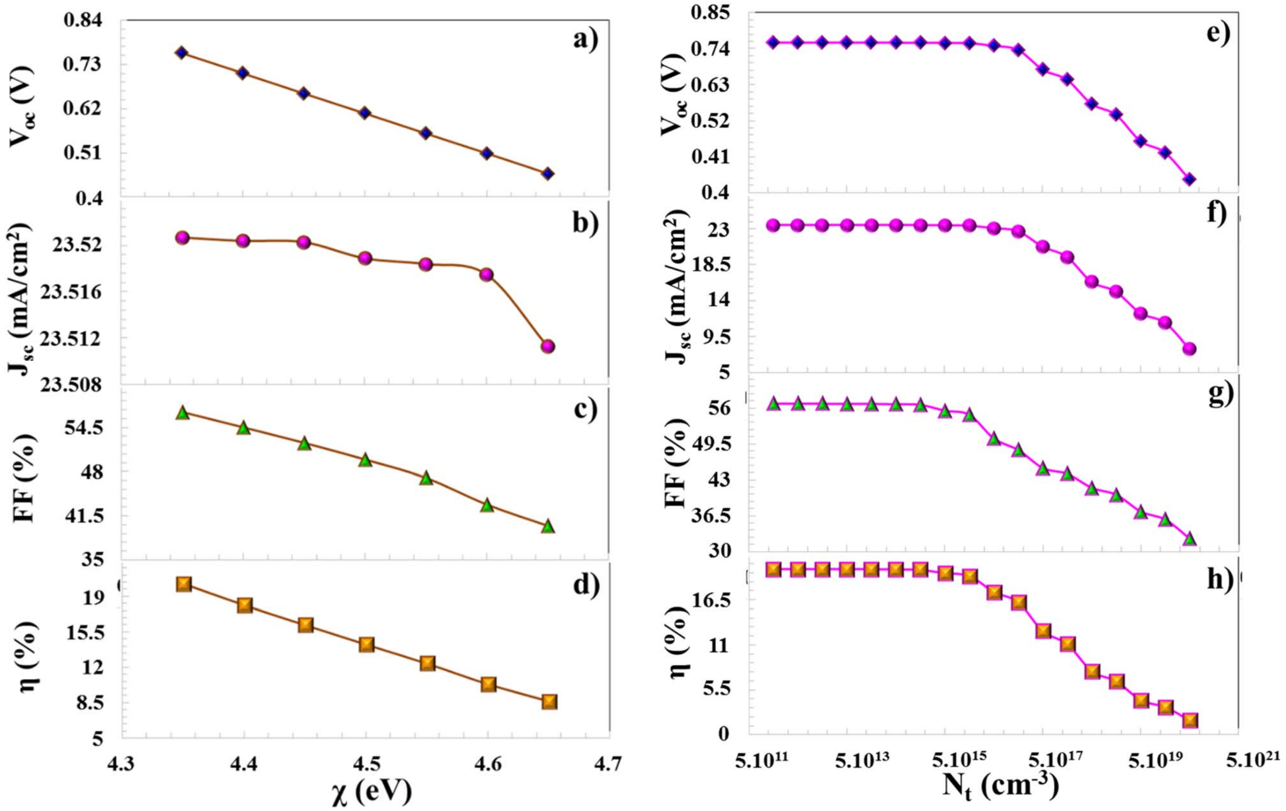

Fig. 4 Variation of PV parameters: V_{oc}, J_{sc}, FF, η as a function of (a–d) χ_e electron affinity (eV) and (e–h) N_t (cm^{-3}).

structure is not ideal or single-level; instead, multiple trap levels of different origins, such as vacancies, antisite defects, interstitial atoms, and grain-boundary-derived defects, are present. These defects create both shallow and deep energy levels within the band gap, complicating carrier transport and recombination mechanisms. In particular, non-homogeneous defect distributions can cause local potential fluctuations in intragrain and grain boundary regions, leading to spatial variation of the electric field and disordered carrier transport. Their defect impact on device performance is usually described *via* the SRH recombination model. SRH recombination occurs when electrons and holes recombine through localized defect states within the band gap of a semiconductor.[34] SRH recombination involves electron–hole pairs recombining through trap states located within the semiconductor's energy gap. Typically centered at mid-gap, an electron from the conduction band occupies the defect energy level (E_t), where it recombines with a valence-band hole, releasing energy as a photon. The solar cell's short-circuit current density (J_{sc}) is adversely affected by increasing neutral defect concentrations (N_t), as the carrier lifetime shortens. The corresponding SRH trap-assisted recombination process is described in eqn (8):

$$R = \frac{np - n_i^2}{\tau_p\left(n + N_C\,e^{\frac{(E_g - E_t)}{k_B T}}\right) + \tau_n\left(p + N_V\,e^{\frac{(E_t)}{k_B T}}\right)} \tag{8}$$

p and n indicate the densities of free holes and electrons within a semiconductor, while E_t denotes the energy levels of trap-related defects. The defect density specified in eqn (9) acts as a fundamental parameter controlling the recombination rate (R).[35] Electron and hole effective lifetimes, represented by τ_n and τ_p, respectively, can be determined through the relation given in eqn (9).[36]

$$\tau_{n,p} = \frac{1}{\sigma_{n,p}\nu_{th}N_t} \tag{9}$$

$$L_{n,p} = \sqrt{\frac{\mu_{n,p}k_B T}{q}\tau_{n,p}} \tag{10}$$

Capture cross-sections for electrons and holes are expressed as $\sigma_{n,p}$, while N_t and ν_{th} correspond to trap density and carrier thermal velocity. The relationship between carrier lifetime and diffusion length is provided in eqn (10). μ_e and μ_p describe the carrier mobilities of electrons and holes, respectively, and q represents the elementary charge inherent to these carriers. These expressions suggest that higher defect concentrations in the semiconductor act as efficient recombination centers, resulting in shorter carrier lifetimes and a subsequent decline in solar cell efficiency.[35,37,38] No significant changes in solar cell performance were detected for N_t values spanning from 1×10^{12} cm^{-3} to 5×10^{15} cm^{-3}, suggesting a stable operational regime. Since the carrier lifetime and diffusion length remained sufficiently high, no significant change in device performance was observed. Electrons and holes formed in this region can reach the junction region without significant trapping or recombination and can be effectively collected. A substantial increase in defect density from 1×10^{16} cm^{-3} to 5×10^{20} cm^{-3}[39] results in a marked reduction in device performance, with V_{oc}, J_{sc}, FF, and efficiency decreasing significantly to 0.34 V, 7.99 mA cm^{-2}, 32.30%, and 1.75%, respectively, as depicted in Fig. 4(e–h). The increase in N_t increased the density of trap-assisted recombination centers within the absorber layer and caused a significant decrease in electron and hole lifetimes, as shown in eqn (9). Consequently, the carrier diffusion length shortened, photo-excited carriers had difficulty reaching the junction region, and recombination losses increased significantly.

A high level of photo-induced carrier generation is localized near the depletion zone of p-type absorber, with values approaching 3.3×10^{22} (cm^{-3} s^{-1}) at $x = 0.42$ μm, as illustrated in Fig. 5(a). Due to the declining absorption of incident photons toward the back contact, the photogeneration rate is reduced to approximately 9.12×10^{20} (cm^{-3} s^{-1}) at $x = 0$ μm. As depicted in Fig. 5(b), the generation–recombination profile across the active layer indicates that within the defect density interval of 10^{14} cm^{-3} to 10^{16} cm^{-3}, SRH recombination does not exceed the generation rate until N_t reaches to 10^{15} cm^{-3}. The results indicate that above a critical defect density of 10^{15} cm^{-3}, SRH recombination increases significantly, negatively impacting PV efficiency, as seen in Fig. 4(e–h).

2.4.2. The impact of the radiative recombination. In CIGSe solar cells, the radiative recombination mechanism is not limited to ideal band-to-band transitions; it is also influenced by multilevel defect states, band-tail formation, and spatially inhomogeneous carrier distributions. Specifically, grain boundaries, compositional fluctuations, and local potential variations can locally increase or suppress the probability of radiative transitions by altering the spatial overlap of electrons and holes. Therefore, the radiative recombination coefficient (B_r) exhibits complex behavior related to defect distribution and local electronic structure, rather than being a uniform and constant parameter in real devices. A photon is emitted when an electron recombines with a hole by transitioning from the conduction band to the valence band, a process termed radiative recombination.[40] The efficiency and rate of this mechanism are captured by the radiative recombination coefficient of B_r as described in eqn (11):

$$B_r = \frac{1}{\tau_{\text{n or p,rad}} N_{\text{A or D}}} \tag{11}$$

The radiative lifetimes of carriers, where electrons and holes are described by $\tau_{n,rad}$(s) and $\tau_{p,rad}$(s), respectively.[40] The performance of CIGSe solar cell, in terms of efficiency, was found to be stable and unaffected by changes in B_r over the investigated range (from 10^{-16} cm^3 s^{-1} to 10^{-8} cm^3 s^{-1}), which shows that the rate of radiative recombination is quite low compared to the carrier production rate. Therefore, photo-generated electron–hole pairs dissociate efficiently, and carrier collection losses are minimal. With increasing B_r over the range of 10^{-8} cm^3 s^{-1} to 10^{-1} cm^3 s^{-1},[21,41] the device exhibited a substantial decline in the PV parameters, including a notable drop in V_{oc} (0.434 V), J_{sc} (6.93 mA cm^{-2}), FF (42.98%), and conversion efficiency (2.58%) as seen in Fig. 6(a–d). The enhancement of B_r is associated with shortened carrier lifetimes or reduced carrier concentrations, ultimately leading to a decline in device performance, as shown in eqn (11). Increased radiative recombination reduces the carrier lifetime, causing photo-generated carriers to recombine before reaching the electrodes. In particular, according to eqn (11), the increase in B_r directly corresponds to the reduction in carrier lifetimes. This reduction in carrier lifetime leads to a V_{oc} loss by narrowing the half-Fermi-level separation, while also limiting J_{sc} and FF by reducing the effective carrier density. The recombination rate approaching and even exceeding the production rate in some regions limited net carrier production. This situation particularly weakened the effective charge separation in the absorber layer and reduced the carrier collection efficiency. As a result, the device efficiency dropped to 2.58%.

According to the recombination-position graph shown in Fig. 7, the recombination rate is 3.22×10^{20}, 7.76×10^{21}, 2.77×10^{22}, 3.85×10^{22} (cm^{-3} s^{-1}) for $B_r = 10^{-10}$, 10^{-8}, 10^{-6}, 10^{-4} cm^3 s^{-1} at $x = 0.420$ μm, respectively. For $B_r = 10^{-10}$ and 10^{-8} cm^3 s^{-1}, since the recombination rates are significantly lower than the generation rates, the photovoltaic parameters do not change in this range as demonstrated in Fig. 6(a–d). However, for the range of $B_r = 10^{-6}$ and 10^{-4} cm^3 s^{-1}, since the recombination

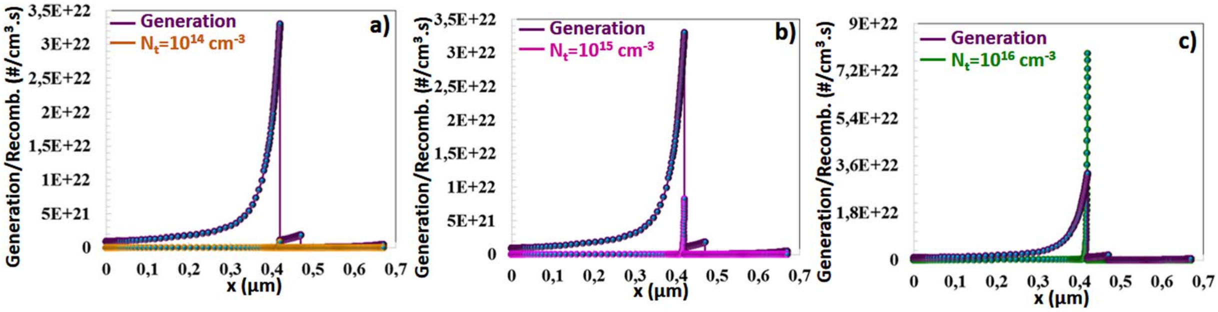

Fig. 5 The position-dependent generation and recombination characteristics of the CIGSe solar cell for defect densities (N_t) ranging from 10^{14} (a), 10^{15} (b), and 10^{16} cm^{-3} (c).

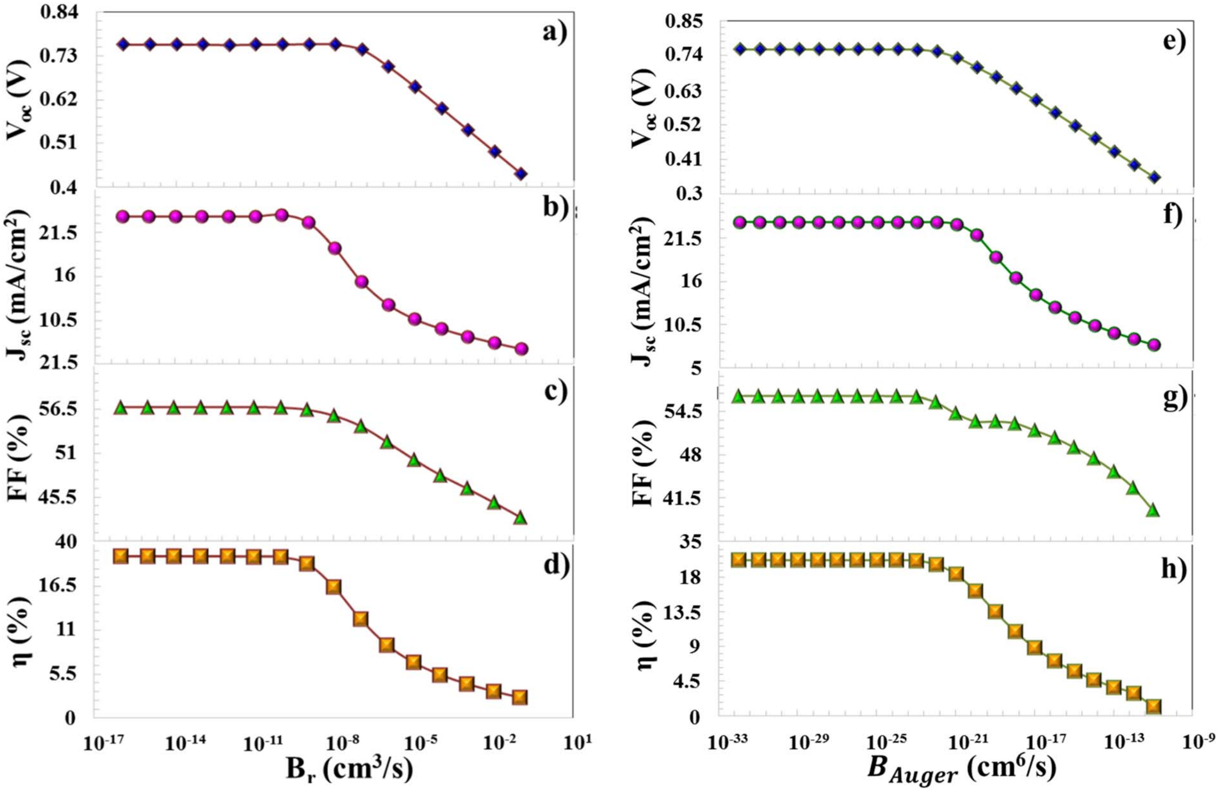

Fig. 6 Variation of PV parameters: V_{oc}, J_{sc}, FF, η as a function of (a–d) B_r ($cm^3\ s^{-1}$) and (e–h) AECC ($cm^6\ s^{-1}$).

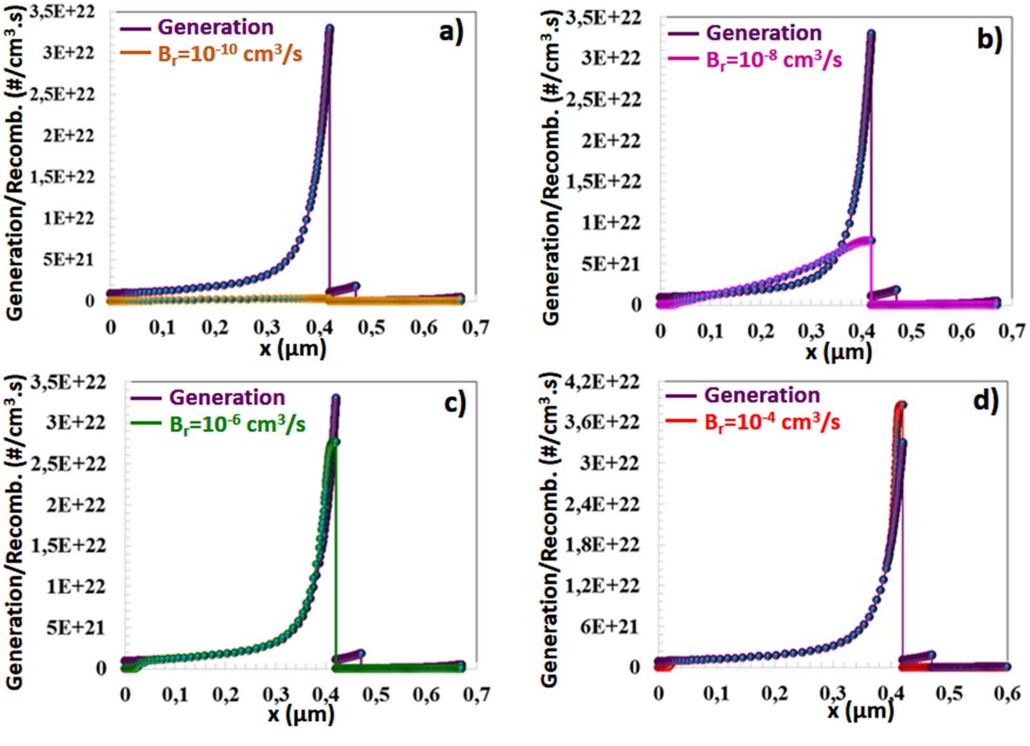

Fig. 7 The position-dependent generation and recombination characteristics of the CIGSe solar cell for the radiative recombination coefficient of (B_r) ranging from 10^{-10} (a), 10^{-8} (b), 10^{-6} (c), 10^{-4} cm^{-3} (d).

rate is close to and sometimes exceeds the generation rate, charge generation is limited, and photovoltaic performance begins to degrade.

2.4.3. The effect of the Auger electron recombination. The recombination of charge carriers within the absorber semiconductor leads to energy release, which is internally transferred to other carriers, facilitating non-radiative excitation to higher energy states, a phenomenon referred to as Auger recombination. Eqn (12) provides the formal definition of the Auger recombination coefficient.[42]

$$B_{\text{Auger,n or p}} = \frac{1}{\tau_{\text{n or p,rad}} {N_{\text{A or D}}}^{2}} \tag{12}$$

This work assessed the solar cell's PV parameters as functions of the Auger recombination coefficient, spanning 10^{-32} cm^6 s^{-1} to 10^{-23} cm^6 s^{-1}, and observed notable deviations in all PV parameters for Auger recombination coefficients up to 10^{-22} cm^6 s^{-1}. As shown in the graph in Fig. 8, in the range 10^{-25} cm^6 s^{-1} to 10^{-24} cm^6 s^{-1},[43–45] the generation rate exceeds the recombination rate, and this does not affect the PV parameters. So, the majority of photocarriers produced in the system reach the junction region without undergoing recombination. Therefore, the production rate remained dominant over the recombination rate, and no significant change in PV values occurred. However, at the value of 10^{-22} cm^6 s^{-1}, since the amount of recombination (2.58×10^{23} (cm^{-3} s^{-1})) significantly exceeds the generation rate (3.3×10^{22} (cm^{-3} s^{-1})), a decrease in PV parameters begins, and the V_{oc}, J_{sc}, FF and efficiency parameters for 10^{-11} cm^6 s^{-1} drops to 0.352 V, 7.94 mA cm^{-2}, 39.68% and 1.22%, respectively. The recombination rate exceeding the production rate led to a significant portion of the carriers formed in the absorber layer being lost before reaching the contacts. This results in a significant reduction in carrier lifetime and a narrowing of the separation between the quasi-Fermi levels. The reduction in quasi-Fermi level separation directly decreases V_{oc}, while the decrease in carrier collection efficiency due to the short diffusion length reduces J_{sc}.[43–45] At the same time, increased internal losses and impaired carrier transport also reduce the FF. Multi-level trap structures and non-homogeneous defect distributions can complicate the effects of Auger recombination. Deep-level defects lead to carrier localization, while carrier–carrier interactions increase in regions with high carrier density, accelerating Auger processes. Furthermore, local potential barriers formed at grain boundaries can restrict carrier transport, leading to additional losses in J_{sc} and FF parameters.[43–45] Although the idealized approach used in the SCAPS model can explain the general trend, spatial heterogeneity and defect-induced local carrier accumulations in real devices can make Auger recombination more pronounced.

2.5. The impact of series and the shunt resistance

The series resistance (R_{s}) and shunt resistance (R_{sh}) are the dominant parasitic resistances in solar cells. (R_{s}) arises from the

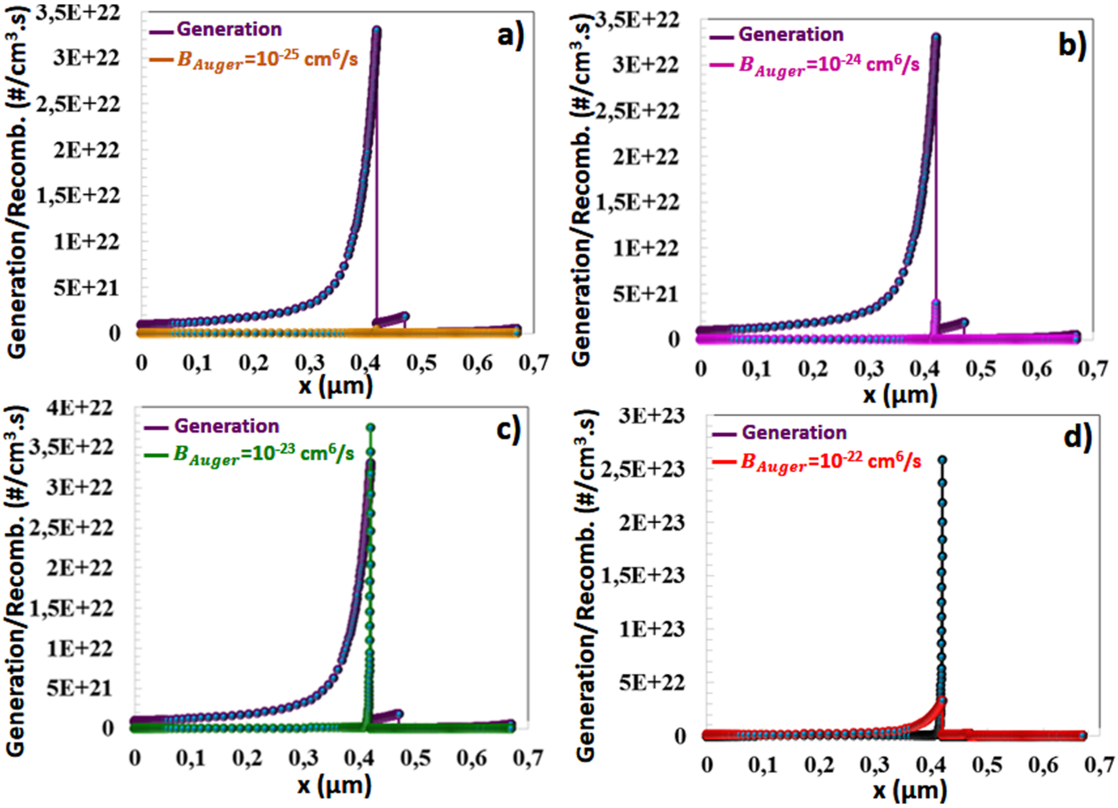

Fig. 8 The position-dependent generation and recombination characteristics of the CIGSe solar cell for the Auger electron recombination coefficients (B_{Auger}) of 10^{-25} (a), 10^{-24} (b), 10^{-23} (c), 10^{-22} cm^{-3} (d).

charge carriers' transport across the semiconductor–metal interface and the cumulative internal resistances within the device.[46] Moreover, the series resistance is governed by multiple factors, including surface grain boundaries, lattice strain, interface trap states, and the intrinsic resistance of the thin-film surface. Shunt resistance fundamentally originates from structural imperfections introduced during thin-film production, including microcracks and pinhole defects,[46] as well as parasitic current pathways and junction-associated leakage mechanisms that collectively degrade device integrity.

The role of R_s and R_{sh} in modulating the fundamental PV characteristics is explicitly captured through the formulation presented in eqn (13):

$$I = I_{ph} - I_o\left[\exp\left(\frac{q(V+IR_s)}{nkT}\right) - 1\right] - \frac{V+IR_s}{R_{sh}} \tag{13}$$

where, I corresponds to the output current,I_o denotes the saturation current, I_{ph} represents the photocurrent, and V signifies the applied voltage, while q, k, n, and T refer to the elementary charge, Boltzmann constant, ideality factor, and absolute temperature, respectively. R_s was systematically reduced from 10 Ω cm^2 to 1 Ω cm^2, while R_{sh} was concurrently varied over a broad range from 1×10^1 Ω cm^2 to 1×10^4 Ω cm^2. Although V_{oc} remains largely unaffected by the decrease in series resistance, a significant increase in J_{sc}, FF, and conversion efficiency is observed, as shown in Fig. 9(a–e). A reduction in ohmic losses, coupled with more efficient charge carrier collection and enhanced current extraction to the external circuit, results in significant improvements in J_{sc}, FF, and overall efficiency. A decrease in R_s from 10 Ω cm^2 to 1 Ω cm^2 led to pronounced increases in J_{sc}, FF, and power conversion efficiency, with values rising from 23.52 to 23.83 mA cm^{-2}, 56.77% to 78.98%, and 20.25% to 28.52%, respectively.[21,47–51] High R_s can disrupt the local electric field distribution within the device. When carriers have difficulty reaching the contacts, accumulation occurs within the absorber, increasing the probability of recombination. Carriers accumulating, especially at grain boundaries, can recombine at trap levels. When the R_s value

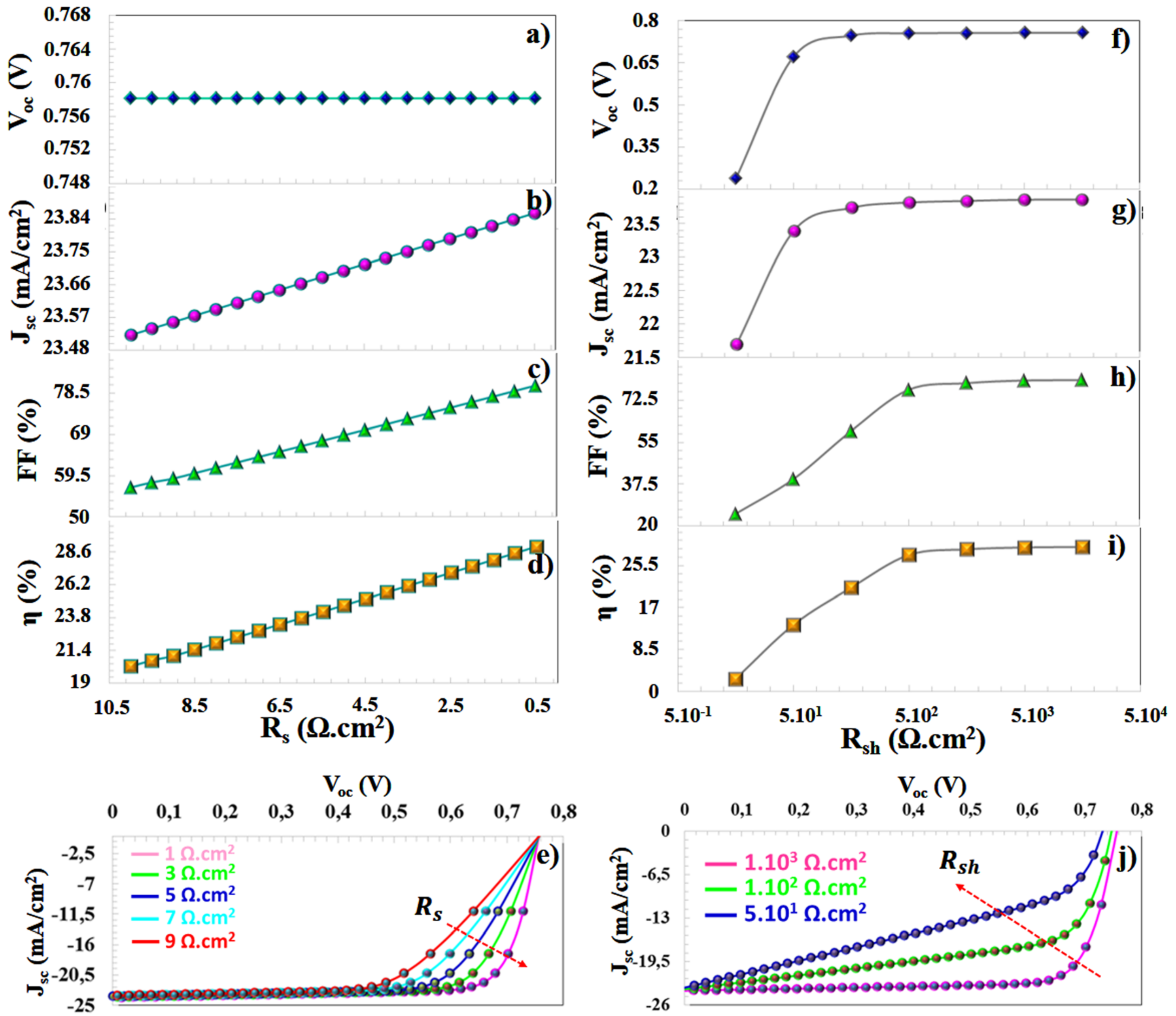

Fig. 9 Variation of PV parameters: V_{oc}, J_{sc}, FF, η as a function of (a–d) R_s (Ω cm^2) and (e–h) R_{sh} (Ω cm^2).

decreases, ohmic losses are significantly reduced, charge carrier accumulation is prevented, and maximum power transfer is improved. Furthermore, the contacts achieve high conductivity, a low-defect crystal structure, a large grain size, reduced grain boundary density, good band alignment, and high-quality metal-back-contact/semiconductor interfaces.

Elevating the shunt resistance reduces current leakage across the shunt path, thereby improving V_{oc} and J_{sc}. This increase also results in notable enhancements of V_{oc}, J_{sc}, FF, and η, as illustrated in Fig. 9(f–l). For the limiting case of an infinitely large shunt resistance, the output voltage can be expressed as follows:

$$V = \frac{kT}{q}\ln\left(\frac{I_{sc}}{I_o}+1\right) \tag{14}$$

As indicated in eqn (14), the output voltage is inversely affected by the magnitude of the reverse saturation current (I_0). A leakage current within the junction can be attributed to sagging bonds, defects, cracks, and pinholes introduced during thin-film deposition. A decrease in shunt resistance directly contributed to the deterioration of all PV device characteristics, as shown in Fig. 9(f–i). Increasing R_{sh} limited parallel leakage current paths within the cell, directing the photogenerated current to the external circuit. This improved V_{oc} and J_{sc} values, particularly in the low-voltage region, by reducing carrier recombination *via* alternating leakage paths. An increase in R_{sh} indicates suppression of ohmic leakage through interface defects, pinhole formation, grain-boundary conductivity, and deposition-induced microcracks. Reducing these leakage paths creates a device characteristic closer to ideal diode behavior and facilitates redirecting photogenerated current toward charge collection rather than recombination.

2.6. The effect of different BSF layers

The BSF in solar cells is formed by a highly doped p-type (p^+) layer at the interface between the rear contact and the light-absorbing layer, acting as a barrier to minimize carrier recombination and enhancing overall device efficiency.[6] It facilitates the directed transport of electrons, minimizing recombination losses and thereby enabling the device to achieve its maximum PV efficiency. Electrons reaching the rear interface of CIGSe solar cells are commonly trapped, limiting their ability to contribute to the generated current (in Fig. 10(a)). The BSF layer facilitates more efficient electron transport by functioning as a quasi-ohmic contact, establishing a modest built-in potential that directs the electrons back, as illustrated in the energy band diagram in Fig. 10(b–d). The BSF layer directs electrons from the conduction band of CIGSe back toward the depletion region, facilitating their effective collection.[11,52] In this manner, even minority carriers are effectively collected at the heterojunction interface rather than lost to recombination at the rear contact, thereby enhancing J_{sc}.

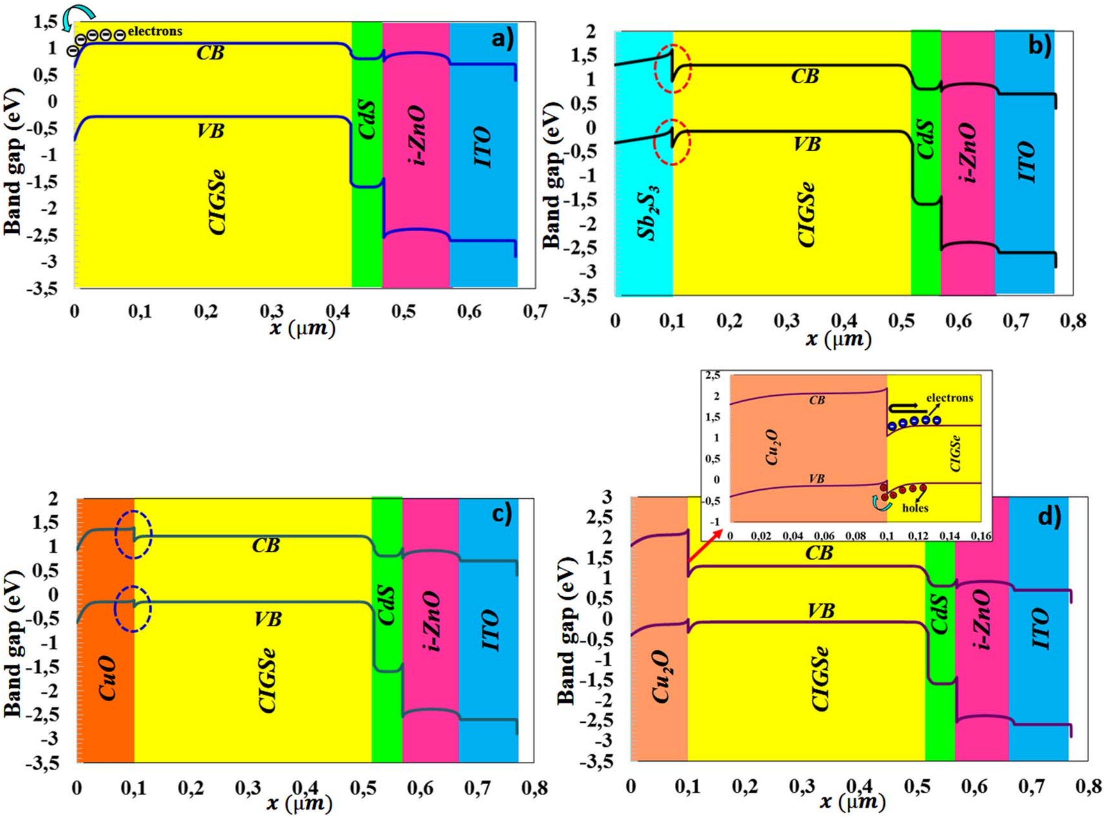

Fig. 10 Energy band diagrams of a Au/CIGSe/CdS/i-ZnO/ITO solar cell illustrating (a) the absence of a BSF layer, and the incorporation of BSF layers composed of (b) Sb_2S_3, (c) CuO, and (d) Cu_2O.

CIGSe-based ultra-thin film solar cells with absorber layers reduced to 420 nm could face limitations in achieving elevated open-circuit voltages. The inherently fragile layers of ultra-thin PV devices mean that even minimal electron losses can significantly impact energy conversion. The implementation of a BSF layer curtails recombination of minority carriers at the rear electrode, enhancing V_{oc} and supporting more efficient collection of photogenerated charges.[53] Optimal band alignment between the BSF and CIGSe layers facilitates smooth hole transport from the absorber to the BSF, reducing carrier losses and improving both V_{oc} and J_{sc}.[11] With well-matched energy levels between the CIGSe and BSF layers, hole transport to the rear electrode becomes more efficient, resulting in minimal losses and reduced recombination, thereby supporting enhanced charge collection and optimal device operation.

As observed in Fig. 11(a), the absence of a BSF layer in the CIGSe solar cell eliminates the back-contact barrier, allowing minority carriers to travel freely to the metal electrode.[4] This facilitates interfacial recombination, thereby reducing device efficiency. In this work, BSF layers comprising Sb_2S_3, CuO, and CuO_2 were incorporated to boost device efficiency, and their corresponding physical parameters are summarized in Table 1. Fig. 10(d) illustrates that the Cu_2O-based BSF layer forms an energy barrier that suppresses minority-carrier flow to the rear contact, redirecting them into the active layer. In contrast, valence-band holes can reach the back contact with negligible recombination losses.

Increasing the BSF thickness enhances the electrostatic field and stabilizes the potential barrier at the p^+-BSF/p-type CIGSe absorber interface, thereby reducing carrier leakage and SRH recombination near the back contact. A thicker BSF also improves back-surface passivation and strengthens carrier separation, which is particularly beneficial for ultra-thin CIGSe absorbers where carriers can easily reach the rear contact. Consequently, carrier collection efficiency increases while back-surface recombination losses decrease. When the Sb_2S_3 BSF layer thickness rose from 10 nm to 100 nm, notable improvements in device performance were observed: V_{oc}, J_{sc}, FF, and η values, which enhanced from 0.695 V to 0.760 V, from 25.45 mA cm^{-2} to 29.84 mA cm^{-2}, from 80.00% to 81.66%, and from 28.33 to 37.05%, respectively (Fig. 11(a–d)). The band gap of 1.62 eV for Sb_2S_3 forms a back face with a wider band than the absorber. The low electron affinity (3.7 eV) creates a repulsive potential barrier for electrons at the CIGSe interface. This reduces recombination by pushing electrons that would otherwise move towards the back contact back into the absorber. The efficiency for an Sb_2S_3 film thickness of 15 nm is approximately 31%, while the yield for a thickness of 20 nm is approximately 33%. The Shockley–Queisser (SQ) limit for a single-junction CIGS solar cell is approximately 30% to 33.7% under standard

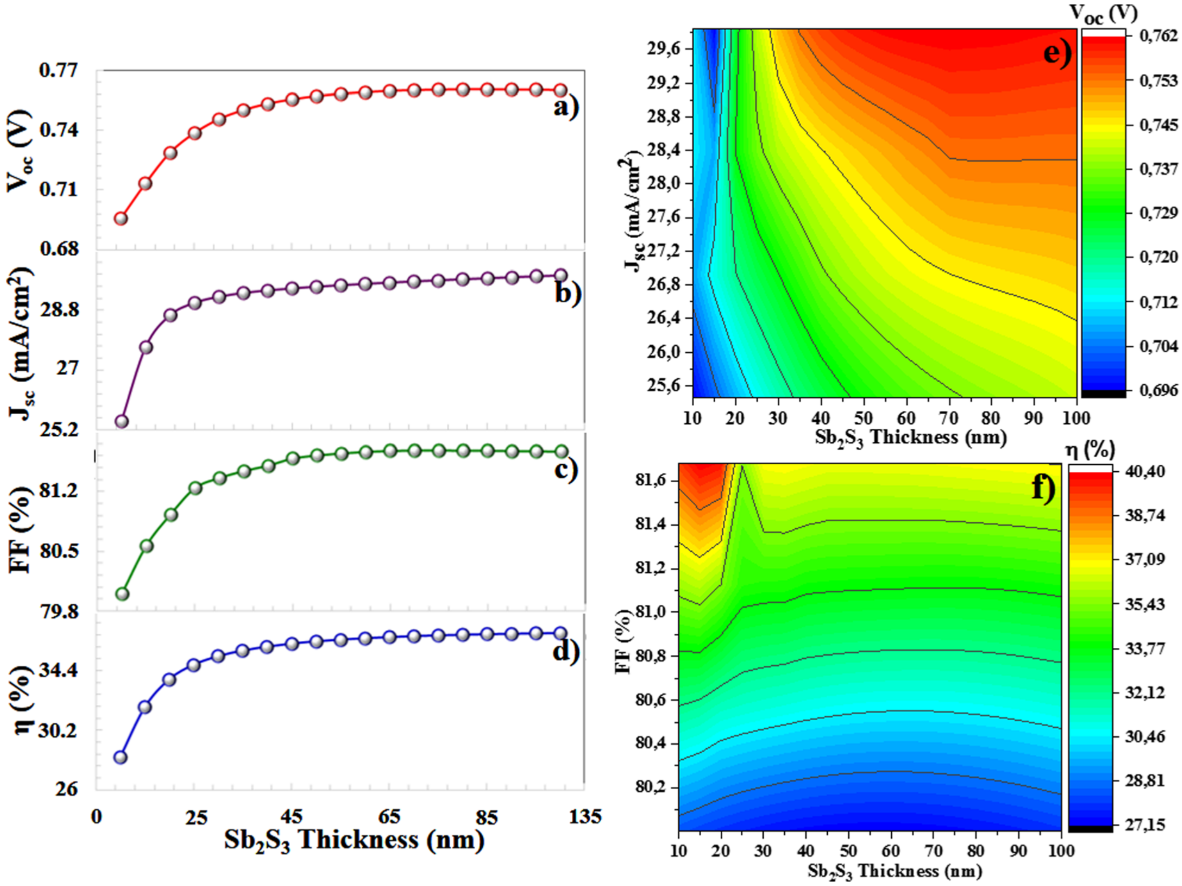

Fig. 11 (a–d) The variation of V_{oc}, J_{sc}, FF, and η, and (e and f) the corresponding contour plots with respect to the thickness of the Sb_2S_3 BSF layer.

AM1.5G solar spectrum conditions. Accordingly, the most realistic value was obtained for 10 nm Sb_2S_3.

J_{sc}, V_{oc}, FF and power conversion efficiency parameters of modelled CIGSe solar cell, based on a heavily doped p-type CuO semiconductor with a 1.51 eV band gap, exhibit an increase from 23.98 mA cm^{-2} to 30.27 mA cm^{-2}, from 0.578 V to 0.660 V, from 77.33% to 79.47%, from 21.44% to 31.76% in Fig. 12(a–d), with increasing CuO BSF thickness from 10 nm 100 nm, respectively. Because the band gap of CuO is lower than that of Sb_2S_3 (1.62 eV), the voltage built-in and barrier height are lower, and some of the incident minority charge carriers may undergo recombination in the back contact region, resulting in somewhat lower performance than that of a solar cell with a Sb_2S_3 BSF layer. CuO exhibits high p-type conductivity, a deep valence band, and a high hole density, facilitating hole transport to the back contact. In addition, CuO has a higher electron affinity (4.07 eV), which reduces the conduction band discontinuity with CIGSe, and electron reflection may not be as strong as in Sb_2S_3. CuO has relatively low hole mobility, which can limit carrier transport and increase series resistance, especially when the BSF thickness increases. Therefore, the solar cell with a CuO BSF exhibits lower PV performance than those with other BSF layers.

Cu_2O exhibits high-doping p$^+$-type semiconductor behavior with a wide band gap (2.2 eV) and high hole mobility. Enhancing the Cu_2O BSF layer thickness from 10 nm to 100 nm significantly improves the performance of the CIGSe solar cell device, yielding increases in J_{sc}, V_{oc}, FF, and power conversion efficiency from 27.57 to 30.03 mA cm^{-2}, 0.595 V to 0.817 V, 77.98% to 82.88%, and 25.35% to 40.34% in Fig. 13(a–d), respectively. The band gap of the Cu_2O layer (2.2 eV) is larger than that of other BSF layers. Therefore, the higher barrier and built-in voltage formed against electrons (photo-excited minority charge carriers) in the active layer generate a larger electrical field, pushing the majority of electrons back towards the depletion region and increasing the amount of charge collection. Cu_2O has the widest band gap (2.2 eV), forming a strong energy barrier in the back region and effectively preventing electrons from reaching the back contact. Because Cu_2O has a wide band gap, it can exhibit low absorption across much of the visible region. Thus, it can reduce parasitic absorption, help long wavelengths remain within the absorber, and increase the optical path length when used with back-reflector structures. Its low electron affinity (3.2 eV) forms a significant conduction band offset with CIGSe ($\Delta E_C = \chi_{CIGSe} - \chi_{Cu_2O}$). This structure reflects minority-carrier electrons back into the absorber, drastically reducing back-surface recombination and providing a strong improvement, especially in V_{oc}. Furthermore, Cu_2O has very high hole mobility, which greatly facilitates hole transport to the back contact and minimizes series resistance

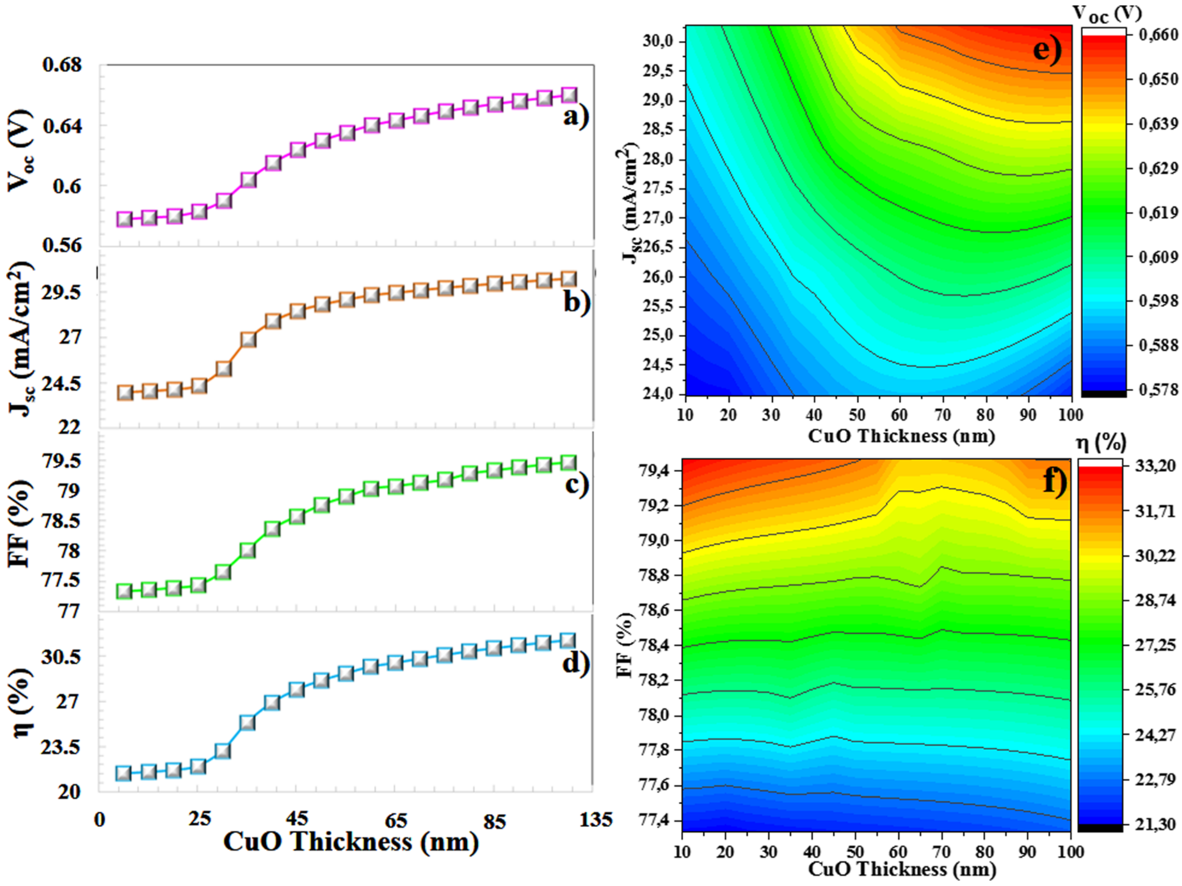

Fig. 12 (a–d) The variation of V_{oc}, J_{sc}, FF, and η, and (e and f) the corresponding contour plots with respect to the thickness of the CuO BSF layer.

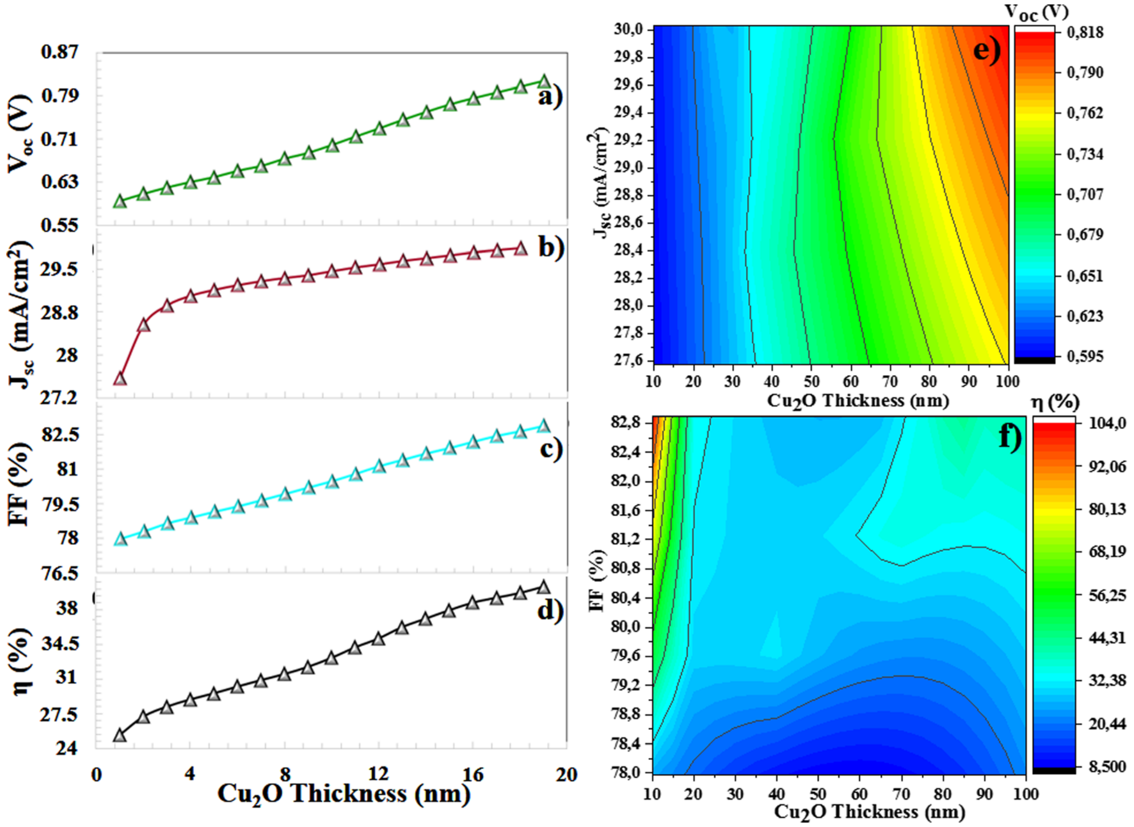

Fig. 13 (a–d) The variation of V_{oc}, J_{sc}, FF, and η, and (e and f) the corresponding contour plots with respect to the thickness of the Cu_2O BSF layer.

losses. High electron mobility also supports carrier transport. Due to the high acceptor density, a strong p^+ field is formed,[54,55] and strong band bending occurs in the back region. Therefore, Cu_2O can exhibit the most effective BSF behavior in terms of both electrostatic field and energy barrier.

The high-efficiency value of CIGSe with Cu_2O BSF, a theoretical result obtained from SCAPS-1D simulation, is not an experimentally verified device performance. The BSF layer acts as a reflective barrier, particularly for minority-carrier electrons, significantly reducing recombination at the back contact. Thus, back surface recombination losses are suppressed, carrier collection efficiency is increased, band alignment becomes more favorable, recombination due to interface defects is reduced, and carrier lifetime and diffusion length are improved. A 35 nm BSF layer provides a partial barrier at the back surface, reducing recombination to a limited extent, and the efficiency is approximately 30%. When the BSF thickness is increased to 55 nm, the band curve and potential barrier become more pronounced, allowing more effective reflection of minority carrier electrons at the back contact. As a result, carrier collection efficiency increases to 35%. At a BSF thickness of 100 nm, back surface recombination is almost completely suppressed, and carrier losses are minimized under ideal simulation conditions. This situation leads to simultaneous increases in J_{sc}, V_{oc}, and the charge factor, bringing the efficiency to approximately 40%. According to the Shockley–Queisser limit, the most realistic value was obtained for Cu_2O thicknesses below 35 nm.

2.7. The effect of interface defect (N_t) between CIGSe and BFS layers on the efficiency of the solar cell

The lattice mismatch between CIGS in a tetragonal phase, Sb_2S_3, CuO, and Cu_2O BSF layers can lead to strain, dislocations, and recombination centers in experimentally produced thin-film solar cells. Increasing the thickness of the BSF may increase the distance carriers travel, leading to carrier scattering, point defects (vacancies, interstitials), grain boundaries, dopant irregularities, composition fluctuations, increased chemical reactions and interdiffusion, decreased conductivity, and, consequently, an increase in R_s. Excessively thick or non-uniform BSF layers may cause pinholes, microcracks, leakage currents, and local recombination losses in real thin-film solar cells. Fig. 14 shows the effect of interface defect density (N_t) (ranging from 1×10^{10} cm^{-3} to 5×10^{17} cm^{-3}) between the Sb_2S_3 and CIGS layers on PV parameters. There is no significant change in PV parameters for $N_t = 1 \times 10^{10}$ cm^{-3} to 1×10^{13} cm^{-3}. However, when N_t increases from 5×10^{13} cm^{-3} to 5×10^{17} cm^{-3}, V_{oc},J_{sc}, FF, and η values drop from 0.760 V to 0.689 V, from 29.84 mA cm^{-2} to 24.24 mA cm^{-2}, from 81.65% to 72.91%, from 37.05% to 24.52%, respectively.

According to Fig. 15, no significant change was observed in the PV parameters of the CIGSe solar cell with CuO BSF layer for $N_t = 1 \times 10^{10}$ cm^{-3} to 1×10^{14} cm^{-3}. When N_t rose from 1.1014 cm^{-3} to 5.1017 cm^{-3}, V_{oc},J_{sc}, FF, and η values decreased from 0.660 V to 0.631 V, from 30.273 mA cm^{-2} to 24.72 mA cm^{-2}, from 79.47 to 70.67%, from 31.76% to 22.77%, respectively. For Sb_2S_3 and CuO

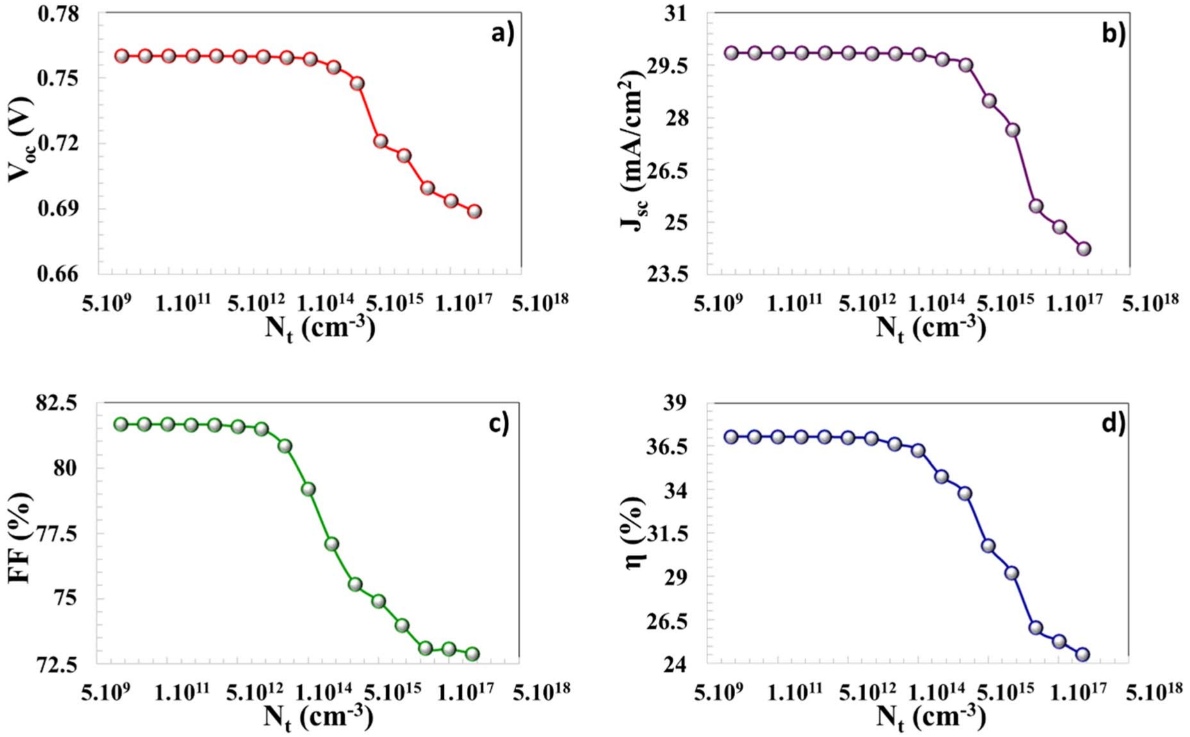

Fig. 14 (a–d) Variation of PV parameters of the CIGSe solar cell with Sb_2S_3 BSF layer: V_{oc}, J_{sc}, FF, η as a function of N_t (cm^{-3}).

BSF layered interface defects, solar cells exhibited similar PV performance. The effect of N_t on CIGSe solar cell with Cu_2O BSF layer is presented in Fig. 16. There is no significant change in J_{sc} values until $N_t = 1 \times 10^{14}$ cm^{-3}. While V_{oc}, J_{sc}, FF and η are 0.815 V, 3030 mA cm^{-2}, 82.88%, 40.34% for $N_t = 1 \times 10^{10}$ cm^{-3}, V_{oc}, J_{sc}, FF and η are 0.503 V, 28.95 mA cm^{-2}, 73.49%, 19.58% for $N_t = 5 \times 10^{15}$ cm^{-3}, respectively. The Cu_2O BSF solar cell was more affected by the N_t value compared to the others (Table 2).

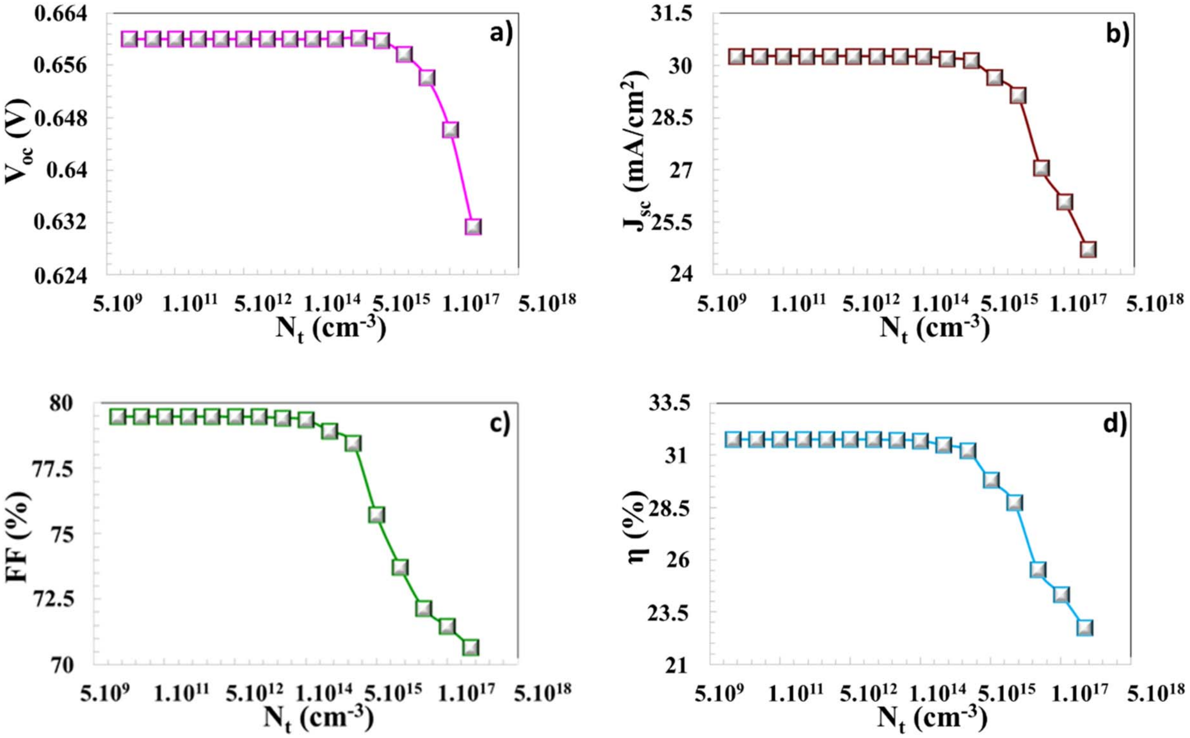

Fig. 15 (a–d) Variation of PV parameters of the CIGSe solar cell with CuO BSF layer: V_{oc}, J_{sc}, FF, η as a function of N_t (cm^{-3}).

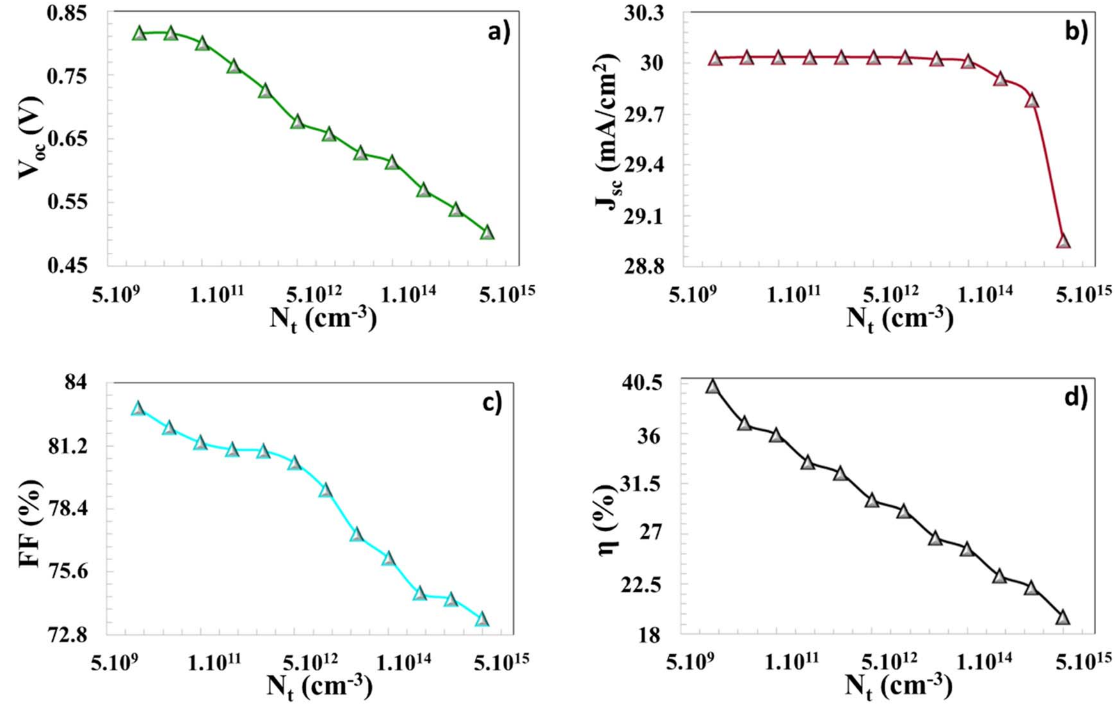

Fig. 16 (a–d) Variation of PV parameters of the CIGSe solar cell with Cu_2O BSF layer: V_{oc}, J_{sc}, FF, η as a function of N_t (cm^{-3}).

Increasing the thickness of the BSF layer can increase the p-type active layer doping differential, which can increase and stabilize the magnitude of the internal electric field formed on the back surface, forming a repulsive force against electrons (minority carriers).[15] It is emphasized that passivating surface defects suppresses recombination by neutralizing active trap states and reinforcing the electric field at the rear junction. A thicker BSF layer enhances the separation between electrons and holes, suppressing recombination, and simultaneously facilitates better carrier alignment, leading to improved charge collection at the electrode. Increasing the thickness of BSF layers from 10 nm to 100 nm improves both charge transport and light absorption, resulting in a notable increase in efficiency. The Fig. 17 shows the J–V curve of a CIGSe solar cell modeled with Sb_2S_3, CuO, and Cu_2O BSF layers. The J_{sc} values of the BSF solar cells are close to each other and high, while the V_{oc} value of the cell with CuO BSF is lower, and that of the structure with Cu_2O BSF is higher. As a result, the highest solar cell efficiency was obtained by a Cu_2O BSF-containing solar cell, according to the J—V characteristic shown in Fig. 17.

The simulated photovoltaic performance parameters obtained from SCAPS-based modeling, both in the present work and in previously reported studies, are comparatively overestimated. This discrepancy arises because SCAPS-1D, owing to its one-dimensional framework, cannot fully account for several critical physical and structural phenomena inherent to experimentally fabricated solar cells. Morphological properties, including lateral carrier transport, grain boundary effects, localized defect states, microcracks, pinhole formation, and surface roughness, are not explicitly accounted for, and all constituent layers are treated as compositionally uniform despite the presence of realistic compositional gradients and doping inhomogeneities in fabricated devices. Intricate defect landscapes and multi-level trapping mechanisms are reduced to simplified representations, while optical phenomena such as light scattering and wave–optical interactions, as well as mechanical stress and thermal coupling effects, are omitted from the model. At material interfaces, processes such as interdiffusion, interfacial chemical reactions, and phase formation are not explicitly resolved, with interface recombination instead approximated through effective defect density parameters. Likewise, non-idealities in metal/semiconductor contacts, including Fermi-level pinning, finite contact resistance, and interfacial roughness-induced transport barriers, are only implicitly treated or neglected. Consequently, the simulated photovoltaic device performance, whether modest or enhanced, remains within the range reported in the existing literature, demonstrating overall consistency with previously published results.

2.8. Capacitance–voltage (C–V) and Mott–Schottky characteristics

The junction's intrinsic properties critically govern the reproducibility of measurements, with the total p–n junction capacitance arising from the additive effects of both depletion and diffusion contributions. Depletion capacitance dominates under reverse bias, while diffusion capacitance prevails under forward bias. C–V characteristic presents the absorber and interfacial mechanisms, enabling precise evaluation of the

Table 2 Comparison of PV parameters of CIGSe thin-film solar cells modeled with the SCAPS-1D program reported in the literature

Solar cell (experimental: E, theoritacal: T, back surfac field: BSF)	V_{oc} (V)	J_{sc} (mA cm^{-2})	FF (%)	η (%)	Reference
Ag/ZnO:Al/i-ZnO/CdS/CIGS/Mo (T)	0.733	36.35	83.33	22.23	56
ZnO:Al/ZnS/CIGSe/Mo (T)	0.693	38.06	83.71	22.11	57
ZTO/CIGS (T)	0.89	36.0	82.0	31.10	58
ITO/CIGS/GaSe (T)	1.62	24.03	94.5	25	59
Zn(O,S)/CIGS/Si/Mo (T)	0.74	39.72	81.94	24.16	60
Mo/CIGS/CdSe/ZnO/ITO (T)	0.983	33.63	75.93	25.11	61
i-ZnO/n-CdS/p-CIGS/Mo (T)	0.80	38.20	75.00	26.15	62
FTO/SnS_2/CIGS/Sb_2S_3/Ni (T)	1.08	33.75	88.50	31.15	63
n-ZnO: Al/i-ZnO/n-ZnS/p-CIGS/Mo (T)	0.82	36.90	85.50	26.00	64
ZnO/CdS/CIGS/Mo (T)	0.78	38.66	80.00	24.45	65
ZnO:Al/i-ZnO/CdS/CIGS/Mo (T)	0.76	32.04	71.47	17.49	66
ZnO:Al/ZnMgOCdS/CIGS/Mo (T)	1.01	34.11	81.66	28.4	67
CIGS (cell) (Cd-free) (E)	0.73	39.58	80.40	23.85	68
ZnO:Al/CdS/CIGS/Mo (E)	0.67	34.90	77.60	18.10	69
ZnO:Al/i-ZnO/CdS/CIGS/Mo (E)	0.73	32.00	—	17.50	66
ZnO/CdS/$CuInGaSe_2$ (E)	0.69	35.50	81.20	19.80	70
ZnO/CdS/PDT-treated CIGS (E)	0.74	37.80	80.60	22.60	71
ZnO:B/i-ZnO/CdS/CIGS/Mo (E)	0.645	36.80	76.00	18.00	72
CIGS/GaAs (BSF)	1.16	43.88	89.52	45.7	73
CIGS/CNGS (BSF)	1.21	32.25	75.0	29.39	13
CIGS/V_2O_5 (BSF)	0.89	41.34	85.8	31.86	74
CIGS/CuO (BSF)	0.96	37.07	83.71	29.88	75
CIGS/Cu_2O (BSF)	0.92	40.40	83.34	31.13	9
CIGS/Cu_2O (BSF)	0.83	36.81	82.73	25.25	55
CIGS/Sb_2S_3 (BSF)	1.08	33.75	88.50	31.15	63
CIGS/CIGS-p^+ (BSF)	1.14	32.61	89.39	33.36	22
CIGS/Cu_2O (BSF)	0.86	40.85	86.69	30.30	54
CIGS/$CuAlO_2$ (BSF)	0.82	35.87	83.11	24.61	7
CIGS/PEDOT:PSS (BSF)	0.86	56.40	80.79	32.83	76
CIGS/SWCNT (BSF)	0.80	42.59	80.38	27.73	8
CIGS/Sb_2S_3 (BSF)	0.760	29.84	81.66	37.05	In this study
CIGS/CuO (BSF)	0.660	30.27	79.47	31.76	In this study
CIGS/Cu_2O (BSF)	0.815	30.30	82.88	40.34	In this study

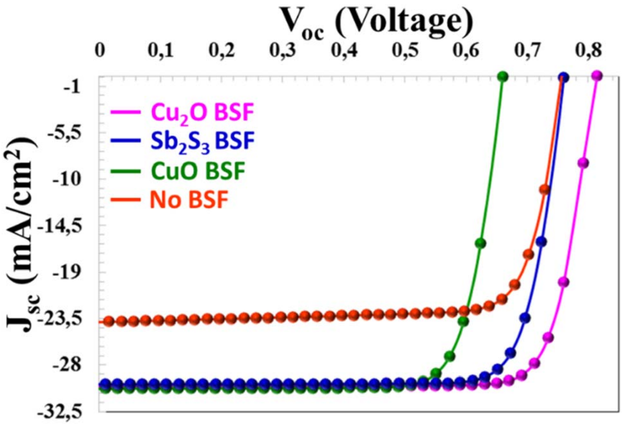

Fig. 17 The dependence of J–V characteristics on BSF layer thickness for CIGSe solar cell without a BSF and with Sb_2S_3, CuO, and Cu_2O BSF layers.

doping concentration (N_a) and built-in potential (V_{bi}) through the subsequent relation:[46,77]

$$\frac{1}{C^2} = \frac{2}{qN_a\varepsilon_o\varepsilon_s A^2}(V_{bi} - V) \tag{15}$$

$$N_a = \frac{2}{q\varepsilon_o\varepsilon_s A^2\left[\dfrac{d}{dV}\dfrac{1}{C^2}\right]} \tag{16}$$

here, N_a denotes the doping concentration (cm^{-3}), q represents the elementary charge (C), and ε_o and ε_s correspond to the vacuum permittivity (8.85×10^{-14} F cm^{-1}) and the material's relative dielectric constant (from Table 1), respectively. A is the active area of the device, C is the capacitance, and V is the externally applied voltage.

The Mott–Schottky analysis is widely recognized as a powerful and reliable method for extracting both the V_{bi} and the doping density of a device. The slope of the $1/C^2$–V relationship in a Mott–Schottky analysis reflects the concentration of electrically active trapping centers.[78,79] C–V and M–S analyses were simulated at a frequency of 10^6 MHz. Fig. 18 presents a detailed examination of (C–V) behavior alongside the Mott–Schottky analysis for the proposed solar cell, highlighting the influence of the shallow, uniformly distributed acceptor concentration (N_a) within the CIGSe absorber layer. The acceptor density (N_a) was systematically adjusted across a range spanning 10^{17} to 10^{18} cm^{-3}. As illustrated in Fig. 18(a), the device capacitance increases progressively with increasing applied bias, ultimately

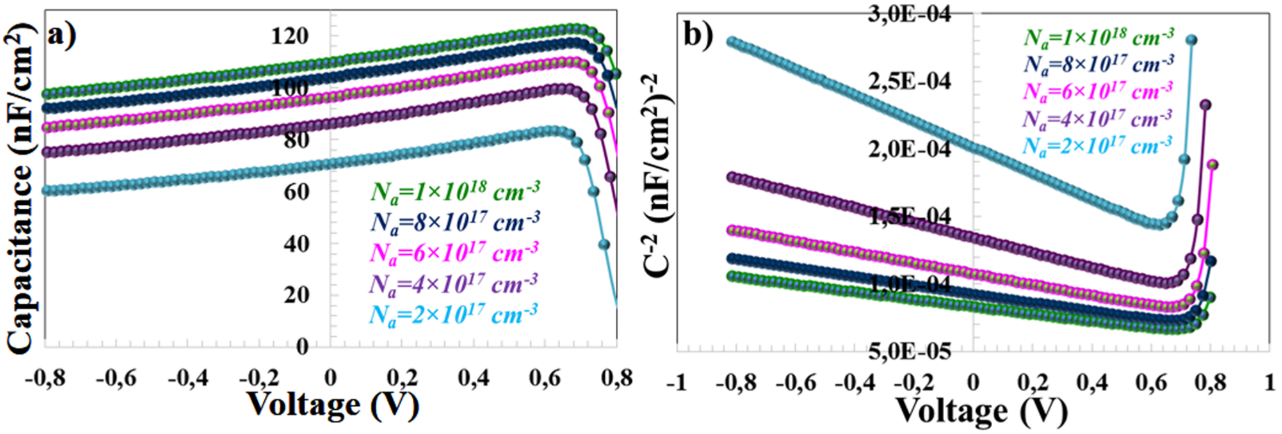

Fig. 18 (a) C–V and (b) C^{-2}–V characteristic depending on N_a variation.

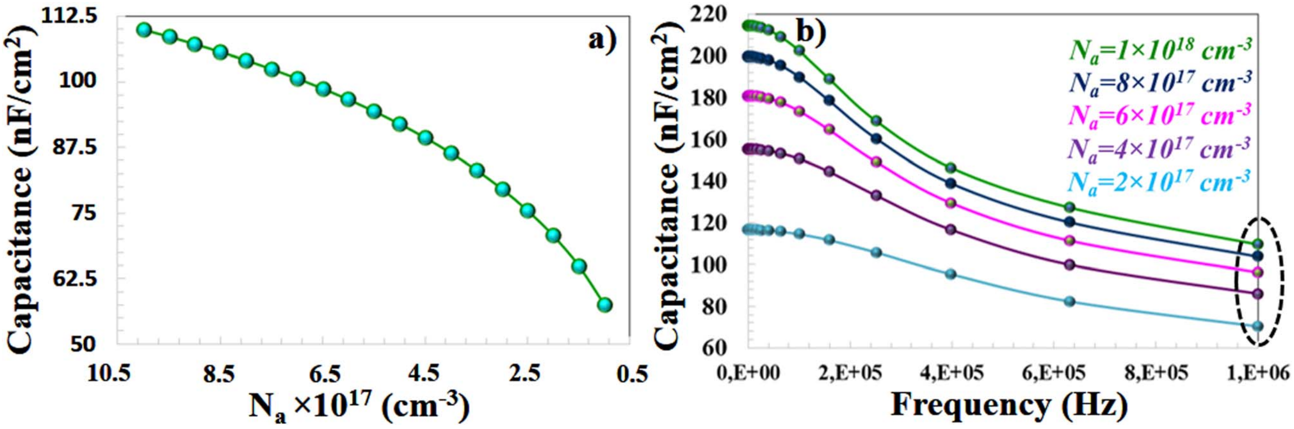

Fig. 19 (a) Capacitance variation and (b) C–f curve depended on N_a value.

reaching a maximum at elevated voltages. Fig. 18(a) shows that the device is fully depleted at zero applied bias. The capacitance value, dependent on N_a, at $V = 0$ is shown in Fig. 19(a). When N_a is increased from 10^{17} to 10^{18} cm^{-3}, the capacitance value increases from 57.57 to 109.94 nF cm^{-2}. Consequently, applying an increasing forward bias gradually increases the capacitance, reflecting the progressive modulation of the depletion region. An increase in doping levels promotes charge buildup at the interface, thereby increasing capacitance. The Mott–Schottky analysis indicates that the built-in potential (V_{bi}) can be extracted from the intercept at $1/C^2 = 0$ on the potential axis in Fig. 18(b). V_{bi} values for $N_a = 1 \times 10^{18}$, 8×10^{17}, 6×10^{17}, 4×10^{17}, and 2×10^{18}, which have been determined to be 0.80, 0.88, 0.96, 1.20, 1.32 eV, respectively. The increase in V_{bi} indicates a more effective internal electric field, facilitating charge separation.

The analysis of C–f characteristics provide valuable insight into the device's electronic behavior and deep defect states, as well as the impact of charge migration on frequency-dependent capacitance and conductance.[46,78] AC signal changes slowly, at low frequencies. Electrons and holes (especially minority carriers) readily follow the signal, and more charge accumulates in the p–n heterojunction. Minority-carrier injection increases, raising the charge density in the junction. However, at high frequencies, the signal changes very rapidly. Electrons and holes cannot keep up with this rapid change. In particular, the minority carrier contribution disappears. Deep defects require time to receive and release charge. Diffusion and injection contributions are lost. Charge accumulation within the p–n junction is limited. This process cannot occur at high frequencies. It is observed that the capacitance values at $V = 0$ in Fig. 18(a) correspond to those measured at 1 MHz in Fig. 19b.[46]

3 Conclusions

In this work, a comprehensive SCAPS-1D simulation of an ultra-thin (420 nm) CIGSe/CdS/i-ZnO/ITO solar cell structure incorporating various p$^+$-type BSF layers (Sb$_2$S$_3$, CuO, and Cu$_2$O) has been systematically performed. The results clearly demonstrate that device performance is highly sensitive to key physical and defect-related parameters. An increase in the acceptor defect density (N_a) from 10^{13} to 10^{18} cm^{-3} significantly enhances the PV response, yielding improvements in V_{oc} (from 0.298 to 0.757 V), FF (from 26.78% to 55.97%), and efficiency (from 3.83% to

19.95%), primarily due to improved carrier concentration and stronger internal electric fields.

Conversely, higher interface defect density ($N_{i\text{–}t} > 10^{13}$ cm^{-3}) and bulk defect density (N_t > 10^{16} cm^{-3}) result in severe recombination losses, drastically reducing device performance. Optimal band alignment was achieved at an electron affinity of $\chi = 4.35$ eV, corresponding to a slight negative conduction-band offset ($\Delta E_c = -0.05$ eV), which minimizes recombination at the heterointerface. Recombination analysis further revealed that radiative recombination remains negligible within 10^{-16} to 10^{-8} cm^3 s^{-1}, while Auger recombination becomes dominant beyond 10^{-23} cm^6 s^{-1}, leading to rapid efficiency degradation. Additionally, reducing series resistance (from 10 to 1 Ω cm^2) and increasing shunt resistance (from 10^1 to 10^4 Ω cm^2) further improved charge collection and minimized leakage losses. Furthermore, capacitance–voltage (C–V) and Mott–Schottky analyses revealed that capacitance increases with N_a (from 57.57 to 109.94 nF cm^{-2} at $V = 0$), indicating enhanced charge accumulation and modulation of the depletion region. The extracted built-in potential (V_{bi}) ranged from 0.80 to 1.32 eV, confirming that the internal electric field strength increases with higher doping levels. Among the investigated BSF layers, Cu_2O exhibited superior performance due to its wider band gap (2.2 eV) and enhanced back surface electric field, achieving a maximum efficiency of 40.34% with $V_{oc} = 0.817$ V, $J_{sc} = 30.03$ mA cm^{-2}, and FF = 82.88%.

Conflicts of interest

The authors declare that they have no known competing financial interests or personal relationships that could have influenced the work reported in this paper.

Data availability

The data supporting this study's findings are available from the corresponding author upon reasonable request.

Acknowledgements

Thanks to Dr Marc Burgelman's group at the University of Gent, Belgium, for allowing us to use the SCAPS-1D simulation program.

References

1 U. C. Matur and N. Baydoğan, Annealing time effect on CIGS thin films, *Emerging Mater. Res.*, 2020, **9**(3), 725–729.
2 X.-D. Chen, *et al.*, Hybrid density functional theory study of Cu $(In_{1-x}Ga_x)Se_2$ band structure for solar cell application, *AIP Adv.*, 2014, **4**(8), 087118.
3 G. Rajan, *et al.*, Characterization and Analysis of Ultrathin CIGS Films and Solar Cells Deposited by 3-Stage Process, *J. Spectrosc.*, 2018, **2018**(1), 8527491.
4 H. Y. H. Al-Buzayd and A. Bahrami, Exploring of inorganic Cu-based back surface field layer on the performance of Sb2Se3/WO3 heterojunction solar cells: A SCAPS-1D simulation study, *Inorg. Chem. Commun.*, 2025, **173**, 113773.
5 M. F. Rahman, *et al.*, Improving the efficiency of a CIGS solar cell to above 31% with Sb_2S_3 as a new BSF: a numerical simulation approach by SCAPS-1D, *RSC Adv.*, 2024, **14**, 1924–1938.
6 A. Houimi, S. Yiğit Gezgin and H. Ş. Kiliç, Theoretical analysis of solar cell performance with different backsurface-filed layers utilizing experimental results of CdS Films deposited by pulsed laser, *Phys. Status Solidi A*, 2022, **219**(11), 2100780.
7 A. Kumar and S. M. Giripunje, A comparative numerical simulation study of CIGS solar cells with distinct back surface field layers for enhanced performance, *J. Phys. Chem. Solids*, 2025, **197**, 112436.
8 A. Kumar, *et al.*, A comprehensive numerical simulation analysis of back surface passivated CIGS solar cells for efficiency enhancement, *Phys. Scr.*, 2025, **100**(3), 035938.
9 A. Kumar, *et al.*, A computational analysis to enhance performance of CIGS solar cells using back surface field and ZnSe buffer layer approach, *Semicond. Sci. Technol.*, 2025, **40**(1), 015014.
10 A. K. Patel, R. Mishra and S. K. Soni, Efficiency improvement of $Cu(In_{(1\text{-}x)}Ga_x)Se_2$ solar cell using copper barium tin sulfide as back surface field layer and bandgap grading technique, *Semicond. Sci. Technol.*, 2024, **39**(1), 015005.
11 B. Barman and P. Kalita, Influence of back surface field layer on enhancing the efficiency of CIGS solar cell, *Sol. Energy*, 2021, **216**, 329–337.
12 M. F. Rahman, *et al.*, A qualitative Design and optimization of CIGS-based Solar Cells with Sn_2S_3 Back Surface Field: A plan for achieving 21.83% efficiency, *Heliyon*, 2023, **9**(12), e22866.
13 E. Oublal, *et al.*, Photovoltaic efficacy of CNGS as BSF and second absorber for CIGS thin film solar cells-numerical approach by SCAPS-1D framework, *Mater. Sci. Eng., B*, 2024, **305**, 117401.
14 S. Y. Gezgin and H. Ş. Kiliç, The effect of Ag and Au contacts on the efficiency of CZTS/n-Si solar cell: the confirmation of experimental and theoretical results by SCAPS simulation, *Braz. J. Phys.*, 2022, **52**(4), 148.
15 R. K. Yadav, *et al.*, A qualitative study of SnSe thin film solar cells using SCAPS 1D and comparison with experimental results: a pathway towards 22.69% efficiency, *Sol. Energy Mater. Sol. Cells*, 2022, **244**, 111835.
16 L. Et-taya, A. Benami and T. Ouslimane, Study of CZTSSe-based solar cells with different ETMs by SCAPS, *Sustainability*, 2022, **14**(3), 1916.
17 S. Y. Gezgin, Modelling and investigation of the electrical properties of CIGS/n-Si heterojunction solar cells, *Opt. Mater.*, 2022, **131**, 112738.
18 S. Yiğit Gezgin and H. Ş. Kiliç, The effect of Ag plasmonic nanoparticles on the efficiency of CZTS solar cell: an experimental investigation and numerical modelling, *Indian J. Phys.*, 2023, **97**(3), 779–796.
19 S. Yiğit gezgin, A. Houimi and H. Ş. Kiliç, Comparison of electrical and photovoltaic parameters of the hetero-

junction solar cells based on CZTS and CIGS ultrathin films, *Mater. Technol.*, 2022, **37**(10), 1573–1585.

20 M. Rafee Mahbub, *et al.*, Simulation of CZTS thin film solar cell for different buffer layers for high efficiency performance, *South Asian Res. J. Eng. Tech.*, 2016, **2**(52), 1–10.

21 Ş. Baturay, *et al.*, Influence of Gd doping on Cu2Sn1-xGdxS3 thin film solar cell, *Iscience*, 2025, **28**(6), 112597.

22 M. Al-Hattab, *et al.*, Numerical simulation of a new heterostructure CIGS/GaSe solar cell system using SCAPS-1D software, *Sol. Energy*, 2021, **227**, 13–22.

23 R. Jaiswal, *et al.*, Numerical study of eco-friendly Sn-based Perovskite solar cell with 25.48% efficiency using SCAPS-1D, *J. Mater. Sci.: Mater. Electron.*, 2023, **34**(8), 753.

24 S. T. Jan and M. Noman, Influence of layer thickness, defect density, doping concentration, interface defects, work function, working temperature and reflecting coating on lead-free perovskite solar cell, *Sol. Energy*, 2022, **237**, 29–43.

25 A. Das, D. P. Samajdar, and B. K. Ravidas, Investigation of the Efficiency of CsGeI 3-based solar cell using SCAPS-1D modeling and simulation, in *2022 IEEE International Conference of Electron Devices Society Kolkata Chapter (EDKCON)*, IEEE, 2022.

26 D. A. Fentahun, A. Tyagi and K. K. Kar, Numerically investigating the AZO/Cu2O heterojunction solar cell using ZnO/CdS buffer layer, *Optik*, 2021, **228**, 166228.

27 F. Islam, *et al.*, Device performance for CTS-based thin film solar cell using Scaps-1D simulator, *J. Sustainability Sci. Manage.*, 2025, **20**(9), 1807–1818.

28 D. L. Khac, *et al.*, Influence/effect of deep-level defect of absorber layer and n/i interface on the performance of antimony triselenide solar cells by numerical simulation, *Sustainability*, 2022, **14**(11), 6780.

29 A. S. Chouhan, N. P. Jasti and S. Avasthi, Effect of interface defect density on performance of perovskite solar cell: Correlation of simulation and experiment, *Mater. Lett.*, 2018, **221**, 150–153.

30 T. D. Veal, *et al.*, Accelerating the development of new solar absorbers by photoemission characterization coupled with density functional theory, *J. Phys.: Energy*, 2021, **3**(3), 032001.

31 S. M. H. Jafari, A. A. Orouji and A. Abbasi, Numerical investigation of ultrathin CIGS solar cells featuring SiO_2/GaAs double rear passivation, *Sci. Rep.*, 2026, **16**(1), 4549.

32 E. Ghorbani, On efficiency of earth-abundant chalcogenide photovoltaic materials buffered with CdS: the limiting effect of band alignment, *J. Phys.: Energy*, 2020, **2**(2), 025002.

33 M. Blankenship, *et al.*, Conduction band cliff at the CdS/$CuIn_{0.1}Ga_{0.9}Se_2$ thin-film solar cell interface, *J. Phys. Chem. C*, 2023, **128**(1), 339–345.

34 S. Bhargav, V. Kumar, and S. Mitta, Machine Learning Based Algorithm for Shockley-Read-Hall Recombination and Augur Recombination Predictions, in *2024 IEEE International Symposium on Smart Electronic Systems (iSES)*, IEEE, 2024.

35 J. Singh, *et al.*, Performance Enhancement of PbS-TBAI Quantum Dot Solar Cell with MoTe2 as Hole Transport Layer, *Phys. Status Solidi A*, 2023, **220**(15), 2300275.

36 F. Baig, *et al.*, Efficiency enhancement of CH 3 NH 3 SnI 3 solar cells by device modeling, *J. Electron. Mater.*, 2018, **47**, 5275–5282.

37 S. Imani, *et al.*, Simulation and characterization of $CH_3NH_3SnI_3$-based perovskite solar cells with different Cu-based hole transporting layers, *Appl. Phys. A*, 2023, **129**(2), 143.

38 R. Malani, T. Pansuriya and V. Kheraj, A study on influence of potential defects and optimization of device structure for CuSbS2 based thin film solar cell using SCAPS-1D simulator, *Opt. Mater.*, 2022, **133**, 112910.

39 F. A. Abega, A. T. Ngoupo and J. Ndjaka, Numerical Design of Ultrathin Hydrogenated Amorphous Silicon-Based Solar Cell, *Int. J. Photoenergy*, 2021, **2021**(1), 7506837.

40 S. R. Hosseini, *et al.*, Investigating the effect of non-ideal conditions on the performance of a planar $CH_3NH_3PbI_3$-based perovskite solar cell through SCAPS-1D simulation, *Heliyon*, 2022, **8**(11), e11471.

41 N. Ahmadi, Device Modeling of Lead-Free Double Perovskite Solar Cell with an Organic Hole Transport Layer, *Trans. Electr. Electron. Mater.*, 2025, **26**(5), 757–764.

42 S. Paul, *et al*, A Simulation Study on Radiative Recombination Analysis in CIGS Solar Cell, in *2017 IEEE 44th Photovoltaic Specialist Conference (PVSC)*, IEEE, 2017.

43 R. T. Prabu, *et al.*, Bandgap assessment of compositional variation for uncovering high-efficiency improved stable all-inorganic lead-free perovskite solar cells, *Phys. Status Solidi A*, 2023, **220**(6), 2200791.

44 J. Chantana, *et al.*, Impact of Auger recombination on performance limitation of perovskite solar cell, *Sol. Energy*, 2021, **217**, 342–353.

45 A. K. Al-Mousoi, *et al.*, Understanding Auger recombination in perovskite solar cells, *Phys. Chem. Chem. Phys.*, 2023, **25**(24), 16459–16468.

46 U. Punia, P. Kumari and S. K. Srivastava, Strategy to achieve> 27.5% efficient PCBM/p-silicon hybrid heterojunction solar cell: Analysis of photovoltaic performances *via* SCAPS-1D, *Silicon*, 2024, **16**(5), 1987–2003.

47 A. Siddique, *et al.*, Numerical modelling and performance investigation of inorganic Copper-Tin-Sulfide (CTS) based perovskite solar cell with SCAPS-1D, *Results Opt.*, 2024, **16**, 100713.

48 S. K. Biswas, *et al.*, Numerical investigation of high efficiency Cu_2SnSe_3 thin film solar cell with a suitable ZnSe buffer layer using SCAPS 1D software, *Eur. J. Electr. Eng. Comput. Sci.*, 2023, **7**(5), 63–70.

49 M. F. H. Bappy, *et al.*, Unveiling the Potential of CTS (Cu_2SnS_3) Solar Cells: High Efficiency and Energy Viability *via* SCAPS-1D Simulation, available at SSRN 5342893.

50 E. L. Meyer, *et al.*, The numerical simulation of a non-fullerene thin-film organic solar cell with Cu2FeSnS4 (CFTS) kesterite as a hole transport layer using SCAPS-1D, *Coatings*, 2025, **15**(3), 266.

51 M. J. Nayeen, *et al.*, Theoretical exploration of high V_{OC} in Cu_2SnS_3 thin film solar cells towards high efficiency, *Sol. Energy*, 2023, **265**, 112076.

52 L. Et-taya, *et al.*, Enhancement of kesterite solar cells using a carbon nanotube as a back surface field layer, *J. Phys. Chem. Solids*, 2025, **196**, 112361.

53 M. Matin, *et al.*, Numerical analysis of novel back surface field for high efficiency ultrathin CdTe solar cells, *Int. J. Photoenergy*, 2013, **2013**(1), 652695.

54 M. R. Sultana, B. Islam and S. R. A. Ahmed, Modeling and performance analysis of highly efficient copper indium gallium selenide solar cell with Cu_2O hole transport layer using solar cell capacitance simulator in one dimension, *Phys. Status Solidi A*, 2022, **219**(5), 2100512.

55 M. H. Yousuf, T. Manzoor and H. U. Manzoor, Empowering Solar Cells With Non-Toxic Cu_2O and Zn (O, S): A Sustainable Approach for CIGS Solar Cells, *Nano Select*, 2026, **7**(1), e70113.

56 A. ul Rehman, *et al.*, A Study on CIGS Thin-Film Solar Cells Through SCAPS-1D Simulations, *Proc. Pakistan Acad. Sci.*, 2025, **62**(1), 81–95.

57 M. Mostefaoui, *et al.*, Simulation of high efficiency CIGS solar cells with SCAPS-1D software, *Energy Procedia*, 2015, **74**, 736–744.

58 R. N. Mohottige, *et al.*, Numerical Simulation of a New Architectural Design of CIGS Thin Film Solar Cell with Zinc Stannate Buffer Layer Using SCAPS-1D, *J. Electron. Mater.*, 2026, **55**(5), 4253–4261.

59 V. Yadav, N. Shrivastav, and J. Madan, Improving the Efficiency of CIGS Thin-Film Solar Cells *via* SCAPs-1D, in *2024 International Conference on Electrical Electronics and Computing Technologies (ICEECT)*, IEEE, 2024.

60 F. Elhady, T. M Abdolkader and M. Fedawy, Simulation of new thin film Zn (O, S)/CIGS solar cell with bandgap grading, *Eng. Res. Express*, 2023, **5**(2), 025027.

61 F. Merad, *et al.*, Performance Optimization of CIGS Thin-Film Solar Cells *via* Charge Transport Layer Engineering: SCAPS-1D Simulations Coupled with Machine Learning, *Results Surf. Interfaces*, 2026, 100813.

62 T. AlZoubi and M. Moustafa, Numerical optimization of absorber and CdS buffer layers in CIGS solar cells using SCAPS, *Int. J. Smart Grid Clean Energy*, 2019, **8**(3), 291–298.

63 M. F. Rahman, *et al.*, Improving the efficiency of a CIGS solar cell to above 31% with Sb_2S_3 as a new BSF: a numerical simulation approach by SCAPS-1D, *RSC Adv.*, 2024, **14**(3), 1924–1938.

64 A. Sylla, S. Touré and J.-P. Vilcot, Numerical modeling and simulation of CIGS-based solar cells with ZnS buffer layer, *Open J. Model. Simulat.*, 2017, **5**(04), 218–231.

65 S. Benabbas, *et al.*, A numerical study of high efficiency ultra-thin CdS/CIGS solar cells, *Afr. J. Sci. Technol. Innov. Dev.*, 2016, **8**(4), 340–342.

66 F. T. Mabvuer, *et al.*, Lowering cost approach for CIGS-based solar cell through optimizing band gap profile and doping of stacked active layers– SCAPS modeling, *ACS Omega*, 2023, **8**(4), 3917–3928.

67 A. Kakade, *et al.*, The Role of Window layers on the simulated performance of CIGS solar cell characteristics using SCAPS-1D, *Next Research*, 2025, **2**(2), 100334.

68 M. Green, *et al.*, Solar cell efficiency tables (version 57), *Prog. Photovoltaics Res. Appl.*, 2021, **29**(1), 3–15.

69 T. Nakada and M. Mizutani, 18% efficiency Cd-free Cu (In, Ga) Se_2 thin-film solar cells fabricated using chemical bath deposition (CBD)-ZnS buffer layers, *Jpn. J. Appl. Phys.*, 2002, **41**(2B), L165.

70 I. Repins, *et al.*, 19.9%-efficient ZnO/CdS/CuInGaSe2 solar cell with 81· 2% fill factor, *Prog. Photovoltaics Res. Appl.*, 2008, **16**(3), 235–239.

71 P. Jackson, *et al.*, Effects of heavy alkali elements in Cu(In, Ga)Se_2 solar cells with efficiencies up to 22.6%, *Phys. Status Solidi RRL*, 2016, **10**(8), 583–586.

72 Y. Hagiwara, T. Nakada and A. Kunioka, Improved J_{sc} in CIGS thin film solar cells using a transparent conducting ZnO: B window layer, *Sol. Energy Mater. Sol. Cells*, 2001, **67**(1–4), 267–271.

73 S. Bhatti, *et al.*, Achieving 45% efficiency of CIGS/CdS solar cell by adding GaAs using optimization techniques, *arXiv*, preprint, arXiv:2309.07551, 2023.

74 M. F. Rahman, *et al.*, Design and numerical analysis of CIGS-based solar cell with V_2O_5 as the BSF layer to enhance photovoltaic performance, *AIP Adv.*, 2023, **13**(4), 045309.

75 A. Kumar, *et al.*, Simulation study of cadmium-free CIGS solar cell for efficiency enhancement by minimizing recombination losses through back surface field mechanism, *Solid State Commun.*, 2024, **394**, 115694.

76 R. Zouache, *et al.*, Numerical Investigation of Enhanced Efficiency in CIGS Solar Cells with 3C-SiC and PEDOT: PSS Integration, *Periodica Polytech., Chem. Eng.*, 2025, **69**(1), 26–34.

77 R. Ranjan, *et al.*, SCAPS study on the effect of various hole transport layer on highly efficient 31.86% eco-friendly CZTS based solar cell, *Sci. Rep.*, 2023, **13**(1), 18411.

78 B. Maharana, R. Jha and S. Chatterjee, Metal oxides as buffer layers for CZTS based solar cells: a numerical analysis by SCAPS-1D software, *Opt. Mater.*, 2022, **131**, 112734.

79 S. K. Biswas, M. K. Mim and M. M. Ahmed, Design and Simulation of an Environment-Friendly ZrS_2/$CuInS_2$ Thin Film Solar Cell Using SCAPS 1D Software, *Adv. Mater. Sci. Eng.*, 2023, **2023**(1), 8845555.